Journal of Engineering Mathematics (2025) 154:1
https://doi.org/10.1007/s10665-025-10477-0

Air cushioning pre-impact dynamics of a wetted body approaching a porous substrate

Gavin Moreton[1,2] · Mark J. Cooker[1] · Richard Purvis[1]

Received: 4 April 2025 / Accepted: 11 August 2025

Abstract
The impact of liquid-coated solid bodies onto porous substrates, or equivalently the impact of porous bodies onto shallow water layers, is considered. This study investigates the role of air cushioning in the pre-impact dynamics of a wetted particle approaching a dry porous medium. By extending a shallow water air cushioning model, we develop an asymptotic theory that couples flow in a lubricating air layer, with an inviscid shallow water film and with Darcy air flow within the porous substrate. Two distinct regimes are identified, namely shallow- and intermediate-depth substrates. The formulated models are solved numerically to determine the influence of substrates on impact pressure, bubble formation, and air escape mechanisms. Numerical results, up to the instant of liquid–substrate impact, reveal that at high porosity the substrate significantly reduces the impact pressure and can suppress bubble entrapment. Permeability is shown generally to hasten the liquid film's descent to the top of the substrate (so-called 'touchdown') as the air gap is closed but, perhaps most surprisingly, porosity can delay touchdown in the regime of shallow porous layers. These findings enhance our understanding of impact mechanics on porous media and offer insights into practical applications such as de-icing technologies and controlled particle adhesion in manufacturing processes.

Keywords Air cushioning · Air jet · Asymptotics · Bubble capture · Impact · Porous substrate · Wet particle

✉ Mark J. Cooker
m.cooker@uea.ac.uk

Gavin Moreton
gtm2@leicester.ac.uk

Richard Purvis
r.purvis@uea.ac.uk

[1] School of Engineering, Mathematics, and Physics, University of East Anglia, Norwich Research Park, Norwich, Norfolk NR4 7TJ, UK

[2] School of Computing and Mathematical Sciences, University of Leicester, University Road, Leicester, Leicestershire LE1 7RH, UK

Published online: 23 August 2025

1 Introduction

The impact of liquid-coated solid bodies or particles onto porous substrates are scenarios of significant interest across many scientific and engineering disciplines. These range from industrial applications such as inkjet printing [1], soil erosion prevention [2, 3] to natural processes like seed dispersal, and the fate of volcanic ash clouds [4]. Another broad context is the action of a breaking sea wave, which can transport a load of solid debris and air in temporary suspension. In coastal waters, the sea wave and its solid particles can violently impact a seawall, which is usually porous, causing damaging collision forces. Including trapped air and wall porosity continues to be a modelling difficulty or an expensive addition to computing such flows. See [5].

Of particular motivation for the current work is aircraft icing in which, as an aircraft flies through clouds, droplets, and ice particles—some of which may be partially melted—impact upon the wings and engine intakes, causing ice growth and possibly a loss of lift or control [6]. Meltwater may also coat the wing and this surface is subject to the impact of naturally occurring solid particles. Recent developments in de-icing and anti-icing approaches have shifted from using traditional mechanical processes (an inflatable boot at the leading edge of the wing that removes ice build up), and thermal techniques (preventing formation or removing formed ice using hot engine air or heater matts), to instead investigating engineered structured hydrophobic or ice-phobic surfaces [7, 8]. The effectiveness of such surfaces has been demonstrated for low-impact speeds, but it remains unclear at higher speeds where water can significantly penetrate into the substrate. Whilst much work on icing prediction has focussed purely on droplet impacts and subsequent splashing [9], there is an increasing awareness that ice particles are also critical in understanding and predicting the threat [10, 11]. An open question around ice particles, and of critical importance in engine intakes, is do they rebound or stick to a surface after impact? [12].

Other scenarios include, for example, in food manufacture, when sprinkling moist seeds (porous or not) onto edible substrates (porous or not) do they stick? It also includes airborne ash. The very complicated fractal-like surface of sub-millimetre-scale ash particles presents a region of flow which can be modelled as a porous layer—porous to both air and any liquid film on an aircraft wing or other surface. The scientific investigation of these phenomena includes the question: Does a particle fragment, melt, bounce, or stick? Answers depend on the micro-mechanics of impact, which in turn is sensitive to the size, depth, and porosity of both the incident particle and the substrate struck.

Air cushioning prior to liquid–solid impacts has been much studied in recent years, with experimental investigations highlighting substantial deformation of a liquid surface just prior to impact and associated bubble entrapment (see [13–16] amongst a wide body of literature). Various theoretical models, usually based on lubricating air flow, have been proposed to explain deformation and predict bubble sizes, originating with [17] for purely inviscid models and with [18] for study of viscous effects and then extended to include surface tension ([19, 20]), compressibility effects [21, 22], porous [23], and flexible substrates [24, 25], amongst many other features. Of particular interest in the current study is how does air cushioning affect a solid particle (coated in a thin liquid film) impacting onto a porous substrate? Marked improvements

in high-speed cameras have allowed much more detailed experimental investigations of liquid impacts onto porous or structured substrates to be carried out [26–32]. In particular, these studies demonstrate that porosity can significantly reduce splashing. However, mathematical studies of such phenomena are comparatively sparse, leaving gaps in understanding of the underlying mechanics.

The current work looks to extend the shallow water cushioning model originally detailed in [33], to include the influence of an unsaturated porous substrate on the impact of liquid-coated particles. This has significance on its own, as suggested above, not least in the distinct behaviour identified when compared with droplet impact cushioning. We also expect our work to lead to better theoretical descriptions and physical insights into liquid impacts onto porous media, which are currently little understood (see [34, 35]). In particular, the simpler model of a water layer presented here (in contrast to the one for generic water-entry or droplet impacts [23]) offers perhaps greater opportunity to understand the transition between pre-impact cushioning, post-impact spreading, and splashing (see also [36] and Ross and Hicks [37]). Although our focus in this paper is restricted to impact onto an unsaturated substrate, it is important for understanding impacts onto both saturated and unsaturated porous substrates, including modelling the longer-term mechanics and ultimate fate of impacting particles.

Compared with collision between impermeable bodies, we make a case that introducing porosity to the surface of one body, can change dramatically all of the physical measures of the impact, and some qualitative features too. Two examples from our results: (i) we show a reduction in impact pressure due to the porosity of the substrate and (ii) at high porosities, the substrate can allow air to flee from under the impact and so remove a bubble which would otherwise be caught between the liquid film and the substrate.

Section 2 below describes in detail our modelling approach, building an asymptotically based theoretical model of the air cushioning behaviour. The model simultaneously couples shallow water flow in the liquid film, with a lubricating air layer in the gap and with Darcy flow inside the porous substrate, all driven by the descending solid particle moving very close to and towards the substrate. Two distinct critical limits of properties in the porous substrate are found. Section 3 presents numerical solutions, and a discussion of the predicted behaviour in each of the two identified limiting sub-cases, with particular attention focussed on the differences between droplet impact and the wetted particle impacts considered here. Section 4 offers conclusions, and a discussion of further extensions to our model.

2 Modelling and Theory

2.1 Modelling assumptions

The physical problem is two-dimensional and left-right symmetric in space. See Fig. 1. We describe the approach towards impact of a circular cylinder of radius R, coated with a thin film of water to a uniform depth h^*. The cylinder can stand for any rigid body, and the radius R can stand for the radius of curvature of the body at its point of

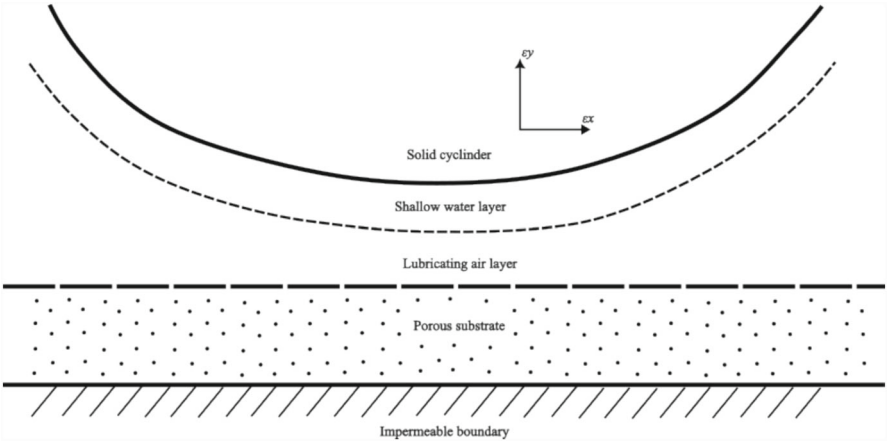

Fig. 1 Diagram showing the various domains of coupled flow. At top is a rigid solid body descending vertically at constant speed. The body is coated in a thin liquid film, whose lower boundary is an air–water interface. The air layer contains a viscous lubrication flow and it in turn lies above a porous substrate whose horizontal upper boundary is permeable to air entering from above or displaced air leaving from below. The substrate's lower boundary is also horizontal and impermeable

first contact. The cylinder descends vertically at constant speed U, in atmospheric air, towards a dry rigid porous substrate. The permeable top surface of the substrate is flat and coincides with the horizontal x^*-axis of coordinates, whose origin is at the centre of incipient impact. The y^*-axis points vertically up, through the cylinder's centre, and is the line of left-right symmetry of the model. Throughout, a star-superscript denotes a variable in physical units. The air-porous substrate lies in the region $-H^* < y^* < 0$, where H^* is its uniform depth and $y^* = -H^*$ is its impermeable bed. The substrate is horizontally unbounded: $-\infty < x^* < \infty$. We assume that the transient air pressure gradients generated by incipient impact allow us to use a Darcy air flow model in the substrate. The substrate is uniform and isotropic, with constant permeability K.

We are interested in a region, with dimensions much shorter than R, close to the origin where the impact pressures are high enough for the following to occur: (a) deform the cylinder's water film surface; (b) push air into and out of the substrate; and (c) displace air already inside the substrate. Prior to the air gap reaching this order of thinness, the velocities and pressure generated in the air are not large enough to affect the liquid flow to leading order due to a typically high viscosity ratio and density ratio of the water and air. A time-dependent air pressure field, $p_a^*(x^*, y^*, t^*)$, is generated by the cylinder as it nears the top of the substrate. The pressure rises dramatically to ever larger magnitudes as time t^* increases towards zero (the instant of liquid–solid impact in vacuo). The local high pressure is associated with the vertical thinning of the lubrication layer, and owing to conservation of mass, there is a horizontal acceleration of the air in the layer. The air layer lies between $y^* = F^*(x^*, t^*) > 0$, and the top of the substrate at $y^* = 0$. The zone of high pressure occupies a small region near the origin. We will find that the air layer and water layer pressure fields share the same scalings for their magnitude (and their extent and duration).

Throughout, we use subscripts a, w, and s to mark variables describing the air, water, and substrate flows, respectively.

For wetted ice or other solid particles, radius R is in the range 0.1 mm to 1 cm. The water film depth, h^*, is typically only 1–3% of R. For wetted ice we envisage a temperature range of 0–20 °C, a feature which affects the range of values of viscosities of air and water. See Section 2 and Appendix A3 of Korobkin et al. [33].

If c denotes the speed of sound in the fluid, then we assume that the Mach numbers U/c in air and water are both much less than unity. Typical impact speeds are in the range 10–30 m/s, making $Ma < 0.1$ for air and $Ma < 0.002$ for gas bubble-free water. A more appropriate measure of the importance of compressibility in the thin air layer is the ratio of the pressure increase in the gas induced by the approaching impact to the ambient gas pressure (see Mandre et al. [38] or [22], for example). By this measure, compressibility may be significant at the higher end of our velocity range. However, for simplicity, we assume the gas is incompressible here, and as such we exclude compressibility from our analysis of the Navier–Stokes equations for both the air and water flows. Compressibility has been incorporated by Mandre et al. [38] and Hicks and Purvis [22] for higher impact speeds into related models for deeper water. If compressibility were included, we would expect the main difference to be slightly smaller trapped bubble sizes.

The density ratio for air and water, ρ_a/ρ_w, is so small that we can use it to help us argue for a neglect of inertia at relevant points whilst establishing our model equations below.

On the air–water interface, we neglect capillarity, owing to the large value of the Bond number $Bo = (\rho_w - \rho_a)R^2 g/\gamma_0$ for an interface between air and water of surface tension coefficient γ_0. For a body with radius of curvature $R = 10^{-2}$ m, we have $Bo = 50$. In addition, our small time scale is not part of the Bond number's definition—during the brief time of impact any surface tension force has little time to move the interface compared with other interfacial stresses which we include in the model. We also assume that near the site of impact the water surface's slope is small and that its vertical displacement is a negligible fraction of both the depth of water and the thickness of the air layer below it.

We neglect gravity as it is tiny compared with fluid-surface-particle accelerations experienced over short times in this work. The Froude number, $Fr = U/\sqrt{gL}$, is large compared with unity, where L is the combined air–water layer thickness (much shorter than R) and the acceleration due to gravity is g. Alone, gravity has little time to displace the two fluids a significant distance.

The viscosity of the air is important and we show that the air flows as a lubrication layer. The water flow has a Reynolds number, $Re_w = UR/\nu$ (where ν is the kinematic viscosity), which lies in the range 700 to 20, 000 for those particle sizes and speeds that we treat. These large values of Re_w are in accord with our scaling and asymptotic work below, needed to achieve a consistent balance amongst dominant terms and to be able to neglect other relatively small terms. See Korobkin et al. [33].

The cylinder starts its descent from an elevation high enough above the substrate for the air pressure to differ little, initially, from its uniform atmospheric value. But as the cylinder falls and nears the substrate, the increasing air pressure has a growing

influence on the shape of the water surface coating the cylinder. As the cylinder–substrate gap narrows, the air pressure rises locally under the cylinder. The three flow regions of water, air, and the in-substrate air, all become intimately linked together. It is from a description of this three-way interaction that we begin to establish in the next section, ultimately, a set of coupled model equations, along with enough boundary conditions and interfacial conditions to make this initial value problem well posed.

2.2 Model equations

We begin deriving our model equations with a two-dimensional, incompressible form of the Navier–Stokes, for air and water:

$$\mathbf{u}^*_{t^*} + (\mathbf{u}^* \cdot \nabla)\mathbf{u}^* = -{\rho^*}^{-1}\nabla p^* + \nu^*\nabla^2\mathbf{u}^*, \tag{1}$$

$$\nabla \cdot \mathbf{u}^* = 0, \tag{2}$$

where the velocity components of air and water are as follows: ${\mathbf{u}_a}^* = (u^*_a(x^*, y^*, t^*), v^*_a(x^*, y^*, t^*))$ and ${\mathbf{u}_w}^* = (u^*_w(x^*, y^*, t^*), v^*_w(x^*, y^*, t^*))$, respectively. On the air–water interface we have the usual kinematic condition and a normal stress condition:

$$v^*_w = F^*_t + u^*_w F^*_x \qquad \text{on} \quad y^* = F^*, \tag{3}$$

$$p^*_w = p^*_a + \sigma \frac{{F^*}_{x^*x^*}}{\left(1 + ({F^*}_{x^*})^2\right)^{\frac{3}{2}}} \qquad \text{on} \quad y^* = F^*, \tag{4}$$

where the water surface under the lower half of the cylinder is $y^* = F^*(x^*, t^*)$. In this work, the Bond number is large enough for us to neglect capillarity. Equation (4) simplifies to equality of pressures: see (11) below.

We assume the porous substrate is isotropic, has constant depth $H^* > 0$, and contains two-dimensional unsteady Darcy flow whose velocity components are given by ${\mathbf{u}_s}^* = ({u^*}_s(x^*, y^*, t^*), {v^*}_s(x^*, y^*, t^*))$, where we interpret the components as air-volume flux per unit cross-sectional area of substrate. These velocity components are governed by

$$u^*_s = -\frac{K}{\mu_a}\frac{\partial p^*_s}{\partial x^*}, \tag{5}$$

$$v^*_s = -\frac{K}{\mu_a}\frac{\partial p^*_s}{\partial y^*}, \tag{6}$$

where K is the dimensional permeability of the medium in units of length squared, and the subscript s indicates variables in the substrate. We expect the pressure and velocity to decay to zero in the far field; that is $\mathbf{u}^*_s \to \mathbf{0}$ and $p^*_s \to 0$ as $|x^*| \to \infty$. At the air-substrate boundary, we assume continuity of air pressure, ${p_a}^*(x^*, 0, t^*) = {p_s}^*(x^*, 0, t^*)$, and continuity of vertical velocity component

${v_a}^*(x^*, 0, t^*) = {v_s}^*(x^*, 0, t^*)$. Regarding the horizontal velocities, from Beavers and Joseph [39], we have a condition linking u_a^* and its normal derivative:

$$\frac{K^{\frac{1}{2}}}{\gamma}\frac{\partial u_a^*}{\partial y^*} = u_a^* - \delta u_s^*, \tag{7}$$

where the dimensionless constant γ is the Beavers–Joseph coefficient, which depends on the medium's pore size and material properties. Also the switch constant δ is such that $\delta = 1$ corresponds to slip, and $\delta = 0$ corresponds to zero-slip on the substrate–air interface. Saffman [40] concluded that u_s^* is directly proportional to K, so that for small K this term is negligible and one can then assume a zero-slip condition. But here, we consider K not necessarily small, and we proceed with the full condition (7).

In summary, we have the following dimensional equations and boundary conditions:

$$\mathbf{u}_{t^*}^* + (\mathbf{u}^* \cdot \nabla)\mathbf{u}^* = -{\rho^*}^{-1}\nabla p^* + \nu^*\nabla^2\mathbf{u}^* \quad \text{in both the air and water,} \tag{8}$$

$$\nabla \cdot \mathbf{u}^* = 0 \quad \text{in both the air and water,} \tag{9}$$

$$v_w^* = F_{t^*}^* + u_w^* F_{x^*}^* \quad \text{on } y^* = F^*, \tag{10}$$

$$p_w^* = p_a^* \quad \text{on } y^* = F^*, \tag{11}$$

$$u_a^* = u_w^* \quad \text{and} \quad v_a^* = v_w^* \quad \text{on } y^* = F^*, \tag{12}$$

$$F^*(x^*, t^*) \to h^* + R - Ut^* - ([R + h^*]^2 - x^{*2})^{\frac{1}{2}} \quad \text{for } t^* \ll -\frac{(R + h^*)}{U}, \tag{13}$$

$$u_s^* = -\frac{K}{\mu_a}\frac{\partial p_s^*}{\partial x^*} \quad -H^* \le y \le 0, \tag{14}$$

$$v_s^* = -\frac{K}{\mu_a}\frac{\partial p_s^*}{\partial y^*} \quad -H^* \le y \le 0, \tag{15}$$

$${p_a}^*(x^*, 0, t^*) = {p_s}^*(x^*, 0, t^*) \quad \text{on } y = 0, \tag{16}$$

$${v_a}^*(x^*, 0, t^*) = {v_s}^*(x^*, 0, t^*) \quad \text{on } y = 0, \tag{17}$$

$$\frac{K^{\frac{1}{2}}}{\gamma}\frac{\partial u_a^*}{\partial y^*} = u_a^* - \delta u_s^* \quad \text{on } y^* = 0, \tag{18}$$

$${v^*}_s(x^*, -H, t^*) = 0 \quad \text{on } y^* = -H, \tag{19}$$

$${\mathbf{u}_s}^*, {p_s}^*, {p_a}^* \to 0 \quad \text{as } |x^*| \to \infty. \tag{20}$$

Next, we simplify the equations by scaling the variables, then neglecting relatively small terms, so making a dimensionless model.

2.3 Non-dimensionalisation

There are many physical parameters in model equations (8–20). So, to make analytical progress, we next non-dimensionalise the relations to help establish which important terms balance and identify the relatively small terms which we can neglect.

First, the velocity scale U drives the flows and induces below the wetted cylinder an air velocity which is much faster horizontally than vertically.

Second, the length scales in the air are ϵR horizontally and $\epsilon^2 R$ vertically, where parameter $\epsilon : 0 < \epsilon \ll 1$ is found explicitly below. Here, $\epsilon^2 R$ is the scale of height of the air gap when the pressures are high enough to deform the liquid–air interface and to force air into the substrate. We define a dimensionless water thickness by writing $h^* = \beta R h(x, t)$ where $h = O(1)$ and $\beta \ll 1$. The scaling of water depth we choose here is the physically interesting case, first studied by Korobkin et al. [33], where the water behaves as a shallow water layer. The two other alternative choices of water layer thickness are as follows: (a) if $h^* \ll \epsilon R$ which reduces to solid–solid impact; (b), if $h^* \gg \epsilon R$ then the flow would be, to leading order, like a droplet (e.g. of radius R), impacting a porous substrate, with no influence from the solid cylinder, as discussed by Hicks and Purvis [23]).

A third consideration for scaling is that in the air layer the significant time scale is $\frac{\epsilon^2 R}{U}$. We defer the correct choice of pressure scaling, in terms of a power of ϵ or β, using dimensional factors P_a and P_w, for which we find expressions below. Consequently, the variables in the water and air layers are scaled by

$$\left(u_w^*, v_w^*, p_w^*, x^*, y^*, t^*, F^*\right) = \left(\frac{\epsilon}{\beta} U u_w, U v_w, \mathcal{P}_w p_w, \epsilon R x, \beta R y, \frac{\epsilon^2 R}{U} t, \epsilon^2 R F\right), \tag{21}$$

$$\left(u_a^*, v_a^*, p_a^*, x^*, y^*, t^*, F^*\right) = \left(\epsilon^{-1} U u_a, U v_a, \mathcal{P}_a p_a, \epsilon R x, \epsilon^2 R y, \frac{\epsilon^2 R}{U} t, \epsilon^2 R F\right), \tag{22}$$

where $\mathcal{P}_w$ and $\mathcal{P}_a$ are dimensional constants that depend on ϵ and or β in ways to be found. The scalings in the water reflect the as yet unspecified thickness of the water layer. Incidentally, the air's horizontal acceleration scale equals the ratio of scales of horizontal velocity to time: $U^2 R^{-1} \epsilon^{-3}$—the smallness of ϵ makes this much greater than acceleration due to gravity.

2.3.1 Equations modelling shallow water flow

The balance of terms that we achieve is supported by the lengthy discussion in Section 2.2 and Appendix 3 of Korobkin et al. [33]. Substitution of the scalings (21) into the governing Eqs. (8) and (9) for water gives

$$u_{wt} + \frac{\epsilon^2}{\beta}\left(u_w u_{wx} + v_w u_{wy}\right) = -\beta \frac{\mathcal{P}_w}{\rho_w U^2} p_{wx} + Re_w^{-1}\left(u_{wxx} + \frac{\epsilon^2}{\beta^2} u_{wyy}\right), \tag{23}$$

$$v_{wt} + \frac{\epsilon^2}{\beta}\left(u_w v_{wx} + v_w v_{wy}\right) = -\frac{\epsilon^2}{\beta}\frac{\mathcal{P}_w}{\rho_w U^2} p_{wy} + Re_w^{-1}\left(v_{wxx} + \frac{\epsilon^2}{\beta^2} v_{wyy}\right), \tag{24}$$

$$u_{wx} + v_{wy} = 0, \tag{25}$$

where the water Reynolds number $Re_w = \rho_w U R/\mu_w \gg 1$. In order to keep a leading order balance here and to match with the flow in the air described below, we are

required to take the pressure scale as

$$\mathcal{P}_w = U^2 \rho_w \beta^{-1}. \tag{26}$$

In order to obtain the leading order shallow water behaviour in the liquid film, this also fixes the size of our water film β as we also need in (23) that $\epsilon^2 \beta^{-1} \ll 1$ and $Re_w^{-1} \epsilon^2 \beta^{-2} \ll 1$. These are equivalent to the pair of double inequalities: $\epsilon^2 \ll \beta$ and $Re_w^{-1/2} \epsilon \ll \beta \ll \epsilon$. Under these assumptions, along with $Re_w \gg 1$, the nonlinear inertial terms and the viscous terms in the governing Eqs. (23) and (24) are negligible.

Assuming that we are within this regime, we obtain for the water flow the linear shallow water equations:

$$u_{wt} = -p_{wx}, \qquad p_{wy} = 0, \qquad u_{wx} + v_{wy} = 0. \tag{27}$$

We have the usual boundary conditions on the water–air interface, namely kinematic condition (10) and normal stress condition (11). The normal stresses must balance so $\mathcal{P}_a = \mathcal{P}_w$. The kinematic condition is

$$v_w^* = F_{t^*}^* + u_w^* F_{x^*}^* \qquad \text{on} \qquad y^* = F^*(x^*, t^*), \tag{28}$$

where $y^* = F^*$ is the air–water interface at the bottom of the shallow water layer. Integrating the continuity equation in (10) with respect to y^* across the shallow water layer (applying the kinematic boundary condition and an impermeability condition on the wall of the body), noting that u_w^* is independent of y^*, we obtain

$$\left[v_w^*\right]_{S^*}^{F^*} = \beta R u_{w_{x^*}}^*, \tag{29}$$

where βR is the average depth of the water layer and $y^* = S^*$ is the impermeable solid surface of the cylinder where $v_w^* = -U$. Substituting in the kinematic condition (28) and rearranging we have

$$F_{t^*}^* + U = \beta R u_{w_{x^*}}^* - u_w^* F_{x^*}^*. \tag{30}$$

Applying the scales (21) we obtain at leading order:

$$F_t + 1 = u_{w_x} \qquad \text{on} \qquad y = F(x, t). \tag{31}$$

We differentiate (31) with respect to t and substitute the horizontal component of (27) to obtain

$$F_{tt} = -p_{w_{xx}} \qquad \text{on} \qquad y = F(x, t). \tag{32}$$

We next show how these model equations for water flow couple with a lubrication flow in the air layer below it.

2.3.2 Equations for the air

The terms of Eqs. (8, 9) for the air layer are scaled using (22) and become

$$\frac{\epsilon^2 \nu_w}{\nu_a}\left(u_{a_t} + u_a u_{a_x} + v_a u_{a_y}\right) = -\frac{\mathcal{P}_a \epsilon^4 \nu_w}{\rho_a \nu_a U^2} p_{a_x} + \frac{1}{Re_w}\left(\epsilon^2 u_{a_{xx}} + u_{a_{yy}}\right), \tag{33}$$

$$\frac{\rho_a}{\rho_w}\left(v_{a_t} + u_a v_{a_x} + v_a v_{a_y}\right) = -\frac{\mathcal{P}_a}{U^2 \rho_w} p_{a_y} + \frac{\rho_a \nu_a}{\rho_w \nu_w Re_w}\left(v_{a_{xx}} + \frac{1}{\epsilon^2} v_{a_{yy}}\right), \tag{34}$$

$$u_{a_x} + v_{a_y} = 0. \tag{35}$$

From Eq. (33), in order to include the final term in a balance with the pressure gradient at leading order, we must have $\frac{\mathcal{P}_a \epsilon^4 \nu_w}{\rho_a U^2 \nu_a} = \frac{1}{Re_w}$. We also know from (26) that $\mathcal{P}_a = \mathcal{P}_w = U^2 \rho_w \beta^{-1}$. These relations give us

$$\frac{1}{Re_w} = \frac{\mu_w}{\mu_a}\frac{\epsilon^4}{\beta}, \tag{36}$$

fixing the small-valued parameter ϵ in terms of other parameters. It also clarifies the validity of the model for β with the inequalities becoming as follows, written in terms of physical variables:

$$\frac{\nu_a}{UR}\left(\frac{\mu_w}{\mu_a}\right)^{\frac{2}{3}} \ll \beta \ll \left(\frac{\mu_a}{UR\rho_w}\right)^{\frac{1}{3}}. \tag{37}$$

These agree with the relationship quoted in Korobkin et al. [33] and can always be satisfied for $Re_w \gg 1$.

Consequently, in (34) the pressure coefficient ($O(\epsilon^{-4})$) is much greater than the $O(\epsilon^{-2})$ coefficient of $v_{a_{yy}}$ in the final term (and in the other terms). As ϵ formally tends to zero, only the pressure gradient term remains. So this term must vanish: $p_{a_y} = 0$; hence, the air layer pressure depends at most on x and t. From now on, we write $p_a = p_a(x, t)$.

We next revisit (33) to check that the leading order terms balance and the other terms are negligible. Using (36, 26), we have

$$\frac{\beta}{\epsilon^2}\frac{\rho_a}{\rho_w}\left(u_{a_t} + u_a u_{a_x} + v_a u_{a_y}\right) = -p_{a_x} + \epsilon^2 u_{a_{xx}} + u_{a_{yy}}. \tag{38}$$

As discussed and exploited by Korobkin et al. [33] (see pp. 371, 388, and their Appendix 3), for air and water the density ratio $\rho_a/\rho_w = O(10^{-3})$ is much smaller than typical $\epsilon = O(10^{-2})$. Therefore, we can neglect the inertia terms of LHS of (38), compared with the lubrication theory balance between the horizontal pressure gradient and the viscous shear force $u_{a_{yy}}$. The remaining term, $\epsilon^2 u_{a_{xx}}$, is also negligible.

Condition (36) tells us the regime of values of physical constants in which we must sit. For air and water $\mu_w/\mu_a \in [50, 100]$ over the temperature range [0, 20 °C] and for fresh water $\rho_a/\rho_w = O(10^{-3})$. We consider U to be in the range 10 to 20 ms^{-1}

and R to be in the interval $[10^{-4}, 10^{-2}\,\mathrm{m}]$. At the lowest end of the range of values of ϵ, we find it takes the value $\epsilon_1 = 0.004$ (large, fast particles), at the highest end $\epsilon = \epsilon_2 = 0.03$ (small, slow particles). We must dismiss the low end of the range of ϵ because the Mach number of horizontal velocity component of flow, $M_a = U/\epsilon_1 c_a$ exceeds unity, at the high end $U/\epsilon_2 = 30\,\mathrm{m/s}$, corresponding to a small Mach number of $Ma = 0.08$. The range of admissible ϵ is narrow but embraces a wide range of values of the physical variables, owing to the nonlinear dependence on ϵ.

Now we choose a mid-range value of $\epsilon = 10^{-2}$ and $\beta = 10^{-3}$ so that $\epsilon^2 \ll \beta \ll \epsilon$. If we also suppose $Re = O(10^3)$ then we satisfy (37). The pressure scale has the high value $\mathcal{P}_a = \mathcal{P}_w = 10^8\,\mathrm{Nm}^{-2}$ which is 1000 bar, over a timescale of 10^{-8} s.

The above is in accord with assuming a large value of the water Reynolds number dictated by (37): $Re_w = \beta\epsilon^{-4}\mu_a\mu_w^{-1} = O(10^3)$.

We now take the leading order terms of Eqs. (38, 35) to make a lubrication model for the air flow:

$$p_{a_x} - u_{a_{yy}} = 0, \tag{39}$$

$$u_{a_x} + v_{a_y} = 0, \tag{40}$$

in the region $0 \le y \le F(x,t)$ in which $p_a = p_a(x,t)$. These equations must be solved subject to a no-slip condition of $u_a = 0$ at $y = F$ (due to scalings (21,22) on the material–particle interface condition (12)), alongside boundary conditions at $y = 0$, which will be discussed below for different substrates.

This completes the model in the air layer above the substrate and below the cylinder's wetting film. However, the flow in the air layer is coupled with the flow across the air–substrate interface. In the next section we look at the air flow into, out of, and inside the dry porous substrate.

2.3.3 Model Equations for the Porous Substrate

We need to link the velocity and pressure in the air layer, at the air–substrate interface. At the bottom of the substrate is an impermeable base. Depending on the depth of the porous substrate, different dynamics can be found. We will model two distinct flow regimes: a shallow substrate and an intermediate-depth substrate. In order to develop the model and complete the boundary conditions for the air lubrication layer, we demonstrate that the thickness of the porous layer is important. We consider two main regimes of layer thickness. First, we have a shallow substrate of dimensionless depth H_{sh}, where $H^* = \epsilon^2 R H_{\mathrm{sh}}$—the substrate's depth is similar to the thickness of the air layer above it. Second, we treat an intermediate-depth regime, where $H^* = \epsilon R H_{\mathrm{in}}$, is comparable to the horizontal extent of the air layer, and where the significant horizontal and vertical dimensions in the substrate flow domain have the same order of magnitude. Also the influence of the impermeable bed is significant in that both velocity components must be included. This second regime can also be extended to treat a third (special) case of a deep porous substrate, $H_{\mathrm{in}} \to \infty$—a situation in which the impermeable bed is too far down to affect the flow over the short timescales considered here.

I—Thin porous layer

We have assumed Darcy air flow in the substrate, Eqs. (14, 15). The flow is driven by balancing the normal component of stress at the substrate's surface, which gives us a boundary condition at $y = 0$:

$$p_s^*(x^*, 0, t^*) = p_a^*(x^*, t^*). \tag{41}$$

Therefore, we must scale the substrate pressure p_s^* in the same way as p_a^* to maintain this balance. We also have conservation of (incompressible) air mass in the substrate (35), which in components is

$$\frac{\partial u_s^*}{\partial x^*} + \frac{\partial v_s^*}{\partial y^*} = 0. \tag{42}$$

We first consider a thin porous layer, whose thickness H^* is comparable to the air layer thickness $\epsilon^2 R$. As such, we scale the substrate variables as follows:

$$\left(u_s^*, v_s^*, p_s^*, x^*, y^*, t^*, H^*\right) = \left(\epsilon^{-1} U u_s, U v_s, \beta^{-1} U^2 \rho_w p_s, \epsilon R x, \epsilon^2 R y, \epsilon^2 \frac{R}{U} t, \epsilon^2 R H_{\text{sh}}\right), \tag{43}$$

where H_{sh} is the dimensionless depth of the substrate domain of flow: $-H_{\text{sh}} \leq y \leq 0$.

These scalings lead to

$$\frac{\partial u_s}{\partial x} + \frac{\partial v_s}{\partial y} = 0. \tag{44}$$

For brevity, we define an effective dimensionless permeability, k:

$$k = \frac{\rho_w U K}{\beta R \mu_a}, \tag{45}$$

so that the scaled velocity components become

$$u_s = -k \frac{\partial p_s}{\partial x}, \tag{46}$$

$$v_s = -\frac{k}{\epsilon^2} \frac{\partial p_s}{\partial y}. \tag{47}$$

For a water layer on a cylinder of radius $R \in [1, 10]$ mm, impact speeds in the range $[1, 10]\,\text{ms}^{-1}$, and substrate permeability of $K = 5 \times 10^{-12}\,\text{m}^2$, we find k lying in the interval $[0.4, 200]$, but we focus on values of $k \sim 1$.

At the interface of the air layer and the porous substrate, the Beavers–Joseph condition (7), scaled and rearranged, gives

$$\frac{k^{\frac{1}{2}}}{\gamma} \frac{\partial u_a}{\partial y} = u_a - \delta u_s \qquad \text{on} \qquad y = 0. \tag{48}$$

Substituting (46,47) into (44), we make a partial differential equation for $p_s(x, y, t)$:

$$\frac{\partial^2 p_s}{\partial x^2} + \frac{1}{\epsilon^2}\frac{\partial^2 p_s}{\partial y^2} = 0, \tag{49}$$

valid in the substrate. At the impermeable bottom of the porous layer $v_s = 0$; therefore, $\frac{\partial p_s}{\partial y} = 0$ is the bed boundary condition for (49) on $y = -H_{\text{sh}}$.

Motivated by the disparate orthogonal length scales in (49) and the approach of Knox et al. [41], we express the substrate pressure in the following asymptotic expansion:

$$p_s(x, y, t) = p_a(x, t) + \epsilon^2 P_s(x, y, t) + O(\epsilon^4), \tag{50}$$

which introduces a new function P_s. The form of (50) is chosen to ensure the leading order pressure matches that in the air layer. We need this so that the normal stresses balance (Eq. (41)) and so that we have a small ($O(\epsilon^2)$) correction term. Substituting (50) into (49), we obtain

$$\frac{\partial^2 p_a}{\partial x^2} + \epsilon^2\frac{\partial^2 P_s}{\partial x^2} + \frac{\partial^2 P_s}{\partial y^2} = O(\epsilon^2). \tag{51}$$

At leading order, we have a relation inside the substrate linking $P_s(x, y, t)$ with the surface pressure $p_a(x, t)$ that drives the flow:

$$\frac{\partial^2 P_s}{\partial y^2} = -\frac{\partial^2 p_a}{\partial x^2}. \tag{52}$$

Noting that the right side of (52) is independent of y, we integrate (52) with respect to y from $y = -H_{\text{sh}}$. In doing this, we use the bottom-impermeability boundary condition (47):

$$\frac{\partial P_s}{\partial y} = -\frac{v_s}{k} = 0 \qquad \text{on} \quad y = -H_{\text{sh}}. \tag{53}$$

From all this, we deduce from (52) that in the substrate

$$\frac{\partial P_s}{\partial y} = -(y + H_{\text{sh}})\frac{\partial^2 p_a}{\partial x^2}. \tag{54}$$

Using this we rewrite the Darcy flow velocity components at the top of the substrate in terms of the air layer pressure, p_a. At the leading order, we have expressions for the two velocity components at $y = 0$:

$$u_s(x, 0, t) = -k\frac{\partial p_a}{\partial x}, \tag{55}$$

$$v_s(x, 0, t) = kH_{\text{sh}}\frac{\partial^2 p_a}{\partial x^2}. \tag{56}$$

Owing to (41,50) and integrating (54) with respect to y, we find the following expression for pressure in the substrate:

$$p_s(x, y, t) = p_a(x, t) - \epsilon^2 \left(\frac{y^2}{2} + H_{\text{sh}} y \right) p_{a_{xx}}(x, t) + O(\epsilon^4). \tag{57}$$

We can now use the expression of velocity in the substrate to complete the model equations in the air layer and link together the unknowns $p_a(x, t)$ and air–water interface position $y = F(x, t)$ when the porous layer is shallow. As derived above, we start with (39, 40):

$$p_{a_x} = u_{a_{yy}}, \tag{58}$$

$$u_{a_x} + v_{a_y} = 0 \tag{59}$$

and follow lubrication theory. We integrate (58) with respect to y twice in the air layer, applying Beavers–Joseph condition (48), and kinematic condition (31) at the air–water interface, at which the horizontal velocity of the air is negligible, to arrive at

$$u_a = \frac{(y - F)\left(\left(\gamma F + k^{\frac{1}{2}}\right) y + k^{\frac{1}{2}} F + 2k\gamma\delta\right)}{2\left(\gamma F + k^{\frac{1}{2}}\right)} \frac{\partial p_a}{\partial x}. \tag{60}$$

We then integrate (40) with respect to y, from $y = 0$ to $y = F$ using (60), and apply the kinematic condition (31). We find:

$$\frac{\partial F}{\partial t} = \frac{1}{12} \frac{\partial}{\partial x} \left(\frac{\gamma F^4 + 4k^{\frac{1}{2}} F^3 + 6k\gamma\delta F^2}{\gamma F + k^{\frac{1}{2}}} \frac{\partial p_a}{\partial x} \right) + k H_{\text{sh}} \frac{\partial^2 p_a}{\partial x^2}. \tag{61}$$

To summarise, the coupled equations for shallow water impact with a porous substrate of thickness H_{sh} and effective permeability k are (61) and

$$F_{tt} = -p_{a_{xx}}. \tag{62}$$

These are complemented by initial and boundary conditions. For large negative times as $t \to -\infty$, we assume the liquid interface is initially undisturbed, so that $F(x, t) = x^2/2 - t$ and that the air gap is initially wide enough that $p_a(x, t) = 0$. We also assume that far enough away from the narrowing gap, the water film and pressure remain unchanged. Hence from (13) expanded in powers of $x^{*2}/R^2 < 1$), we have $F(x, t) \to x^2/2 - t$ and $p_a(x, t) \to 0$, as $x \to \pm\infty$. The principal unknowns of the model in this shallow substrate regime, consist of two self-contained coupled equations for $F(x, t)$, $p_a(x, t)$, and from these $p_s(x, t)$ and the velocity fields can be subsequently found.

In anticipation of the discussion of our results, we introduce further definitions here, see Fig. 2 (left panels). For the entirety of our results discussion we will concentrate solely on the right half of the symmetric domain with $x > 0$. Notice the water layer

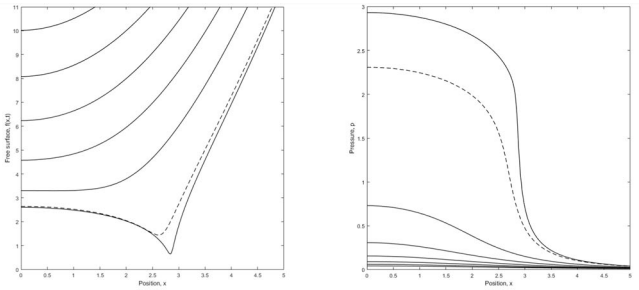

(a) Free-surface and pressure profiles for increasing t as the water layer approaches the substrate. A dashed curve corresponds to $t = 0$, the touchdown time in the absence of air cushioning. Profiles are drawn at times $t = -10, -8, -6, -4, -2, 0$ then $t = 0.25$. Touchdown occurs at $t_0 = 0.36$.

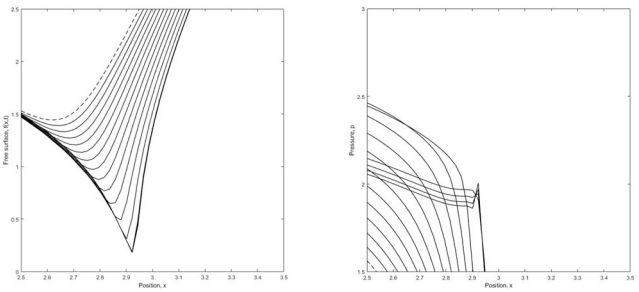

(b) As (a) detail of free surface tongue and nearby pressure close to touchdown. Profiles at $t = 0, 0.025, 0.05, 0.075, ..., 0.325$ before touchdown at $t = t_0 = 0.36$.

Fig. 2 Free surface and pressure profiles during the approach to impact with an impermeable substrate. A dashed curve marks $t = 0$ (touchdown time without air cushioning). **a** Free surface and pressure profiles for increasing t as the water layer approaches the substrate. A dashed curve corresponds to $t = 0$, the touchdown time in the absence of air cushioning. Profiles are drawn at times $t = -10, -8, -6, -4, -2, 0$, then $t = 0.25$. Touchdown occurs at $t_0 = 0.36$. **b** As (**a**) detail of free-surface tongue and nearby pressure close to touchdown. Profiles at $t = 0, 0.025, 0.05, 0.075, ..., 0.325$ before touchdown at $t = t_0 = 0.36$

deforms and descends as a lengthening 'tongue', and this tongue meets the substrate at touchdown time t_0. The horizontal air-volume flux is computed across a movable vertical line segment $x = l(t)$ drawn from the lowest point of the tongue down to the substrate at $y = 0$. The horizontal volume flux, HVF, is defined as

$$\mathrm{HVF}(t) = \int_0^{F(l,t)} u_a(l, y, t)\, \mathrm{d}y, \tag{63}$$

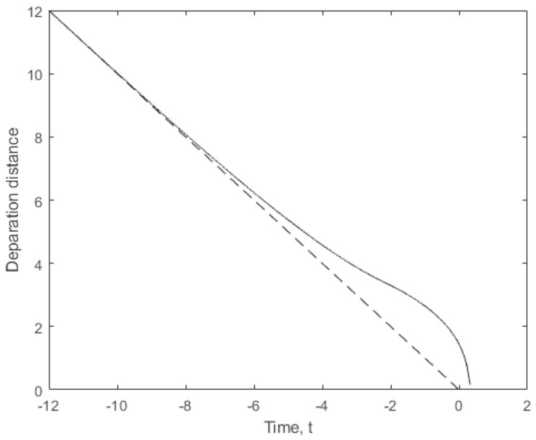

Fig. 3 Impermeable substrate: separation distance between the lowest point on the interface and the top of the substrate plotted as a function of time. The dashed line shows the separation distance for an un-cushioned impact

where $y = F(l, t)$ is the position of the liquid's lower surface. The vertical air-volume flux, VVF, is also defined at the substrate's upper boundary, $y = 0$, via

$$\mathrm{VVF}(t) = -\int_0^{l(t)} v_a(x, 0, t)\, \mathrm{d}x, \tag{64}$$

where $x = l(t)$ is the position of the lowest point on the tongue.

We report in Fig. 10 that the two volume fluxes have similar magnitude whilst growing in time towards their maximum values. Then, whilst the vertical flux continues to rise, the horizontal flux decays to zero at $t = t_0$. (It is a coincidence that the two curves for HVF and VVF cross near $t = 0$.) Physically, the incipient bubble of free air loses gas in two distinct ways:
(i) air escapes horizontally under the tongue (and interacting with the tongue by allowing it to 'skate' on top of the air-lubricating layer) and (ii) escaping air is pushed down into the substrate, where it and the displaced air are constrained by the impermeable bed to move to the right, under the tongue.

II—Intermediate-depth porous substrate

For our second regime, we no longer restrict the substrate depth to be similar to the water layer depth. Instead, we treat a regime in which the depth is comparable to the horizontal extent (ϵR) of the lubrication region. This is the next critical asymptotic balance. As such we write scalings in the substrate as follows:

$$\left(u_s^*, v_s^*, p_s^*, x^*, y^*, t^*, H^*\right) = \left(U u_s, U v_s, \beta^{-1} U^2 \rho_w p_s, \epsilon R x, \epsilon R y, \frac{\epsilon^2 R}{U} t, \epsilon R H_{\mathrm{in}}\right), \tag{65}$$

where H_{in} is a new dimensionless depth of the intermediate-depth substrate. The derivation of the air layer equations is almost unchanged. However, we have a slightly different boundary condition from the Beavers–Joseph condition (7) because the horizontal velocity scale is now the same size as the vertical velocity scale. Upon applying

the scales, the air-substrate boundary condition, at $y = 0$, becomes

$$\frac{k^{\frac{1}{2}}}{\gamma}\frac{\partial u_a}{\partial y} = u_a, \tag{66}$$

where k is defined in (45). (Factor δ is absent from (66) because the term to which it was attached is negligible compared to the dominant terms.) Thus, we find

$$u_a = \frac{(y-F)\left(\left(\gamma F + k^{\frac{1}{2}}\right)y + k^{\frac{1}{2}}F\right)}{2\left(\gamma F + k^{\frac{1}{2}}\right)}\frac{\partial p_a}{\partial x} \qquad \text{for} \quad 0 < y < F(x,t). \tag{67}$$

From the conservation of mass equation and by substituting in the Darcy velocities (5) and (6), we see that the substrate pressure must satisfy Laplace's equation, along with the following boundary conditions: pressure and vertical air velocities are continuous on the air–substrate interface and zero normal velocity component on the impermeable base. Thus we have

$$\nabla^2 p_s(x,y,t) = 0, \tag{68}$$

$$p_s(x,0,t) = p_a(x,t), \tag{69}$$

$$-k\frac{\partial p_s}{\partial y}(x,0,t) = v_a(x,0,t), \tag{70}$$

$$\frac{\partial p_s}{\partial y}(x,-H_{\text{in}},t) = 0, \tag{71}$$

$$p_s \to 0 \qquad \text{as} \quad |x| \to \infty. \tag{72}$$

This problem can be solved using complex analysis techniques. For brevity, the details are in Appendix A. We obtain an integral equation for the unknown vertical velocity in the porous layer, at the substrate surface:

$$v_s(x,0,t) = \frac{1}{\pi}\left(\int_{-\infty}^{\infty}\frac{k\,p_{a\xi}}{\xi - x}\mathrm{d}\xi - \int_{-\infty}^{\infty}\frac{k\,p_{a\xi}(\xi - x) + 2H_{\text{in}}v_s}{(\xi - x)^2 + 4H_{\text{in}}^2}\mathrm{d}\xi\right). \tag{73}$$

$$= V(x,t) \tag{74}$$

We proceed from Eq. (67) in the same way as for a shallow substrate. However, the vertical component of air velocity must satisfy (73) with $v_s(x,0,t) = V(x,t)$ say, so we have the following equation from the air layer theory:

$$\frac{\partial F}{\partial t} = V(x,t) + \frac{1}{12}\frac{\partial}{\partial x}\left(\frac{\gamma F^4 + 4k^{\frac{1}{2}}F^3}{\gamma F + k^{\frac{1}{2}}}\frac{\partial p_a}{\partial x}\right). \tag{75}$$

This is coupled with Eq. (32). However, we now have an explicit dependence on the vertical component of air velocity at the top of the substrate. In order to calculate this we must first solve for the substrate pressure using (68)–(72). This yields a system of coupled equations more complicated than for a shallow substrate.

In summary, the coupled system for a shallow water layer and air impacting onto an intermediate-depth porous substrate, of porosity k and depth H_{in}, is

$$\frac{\partial F}{\partial t} = V(x,t) + \frac{1}{12}\frac{\partial}{\partial x}\left(\frac{\gamma F^4 + 4k^{\frac{1}{2}}F^3}{\gamma F + k^{\frac{1}{2}}}\frac{\partial p_a}{\partial x}\right) \qquad x \in \mathbb{R}; \tag{76}$$

$$V(x,t) = \frac{1}{\pi}\left(\fint_{-\infty}^{\infty}\frac{k p_{a\xi}}{\xi - x}\mathrm{d}\xi - \int_{-\infty}^{\infty}\frac{k(\xi - x)p_{a\xi} + 2H_{\text{in}}V(\xi,t)}{(\xi - x)^2 + 4H_{\text{in}}^2}\mathrm{d}\xi\right); \tag{77}$$

$$F_{tt} = -p_{a_{xx}} \qquad x \in \mathbb{R}. \tag{78}$$

As in the shallow substrate regime, for large negative times, we assume the liquid interface is undisturbed so that $F(x,t) = x^2/2 - t$ and that the air gap is initially wide enough that $p_a(x,t) = 0$. The principal unknowns of the model, in this regime, are $F(x,t)$, $p_s(x,y,t)$, $p_a(x,t)$ and from these the velocity fields can be found. There are three parameters: k, $k^{1/2}\gamma^{-1}$, and H_{in}. In the numerical investigation that follows we fix γ, pick $\delta = 1$, and vary k and H_{in}.

In order to investigate the limiting case of an infinitely deep porous layer, we simply take the limit as $H_{\text{in}} \to \infty$ in (73) to obtain the effect of the substrate on the air. The second integral of (73) then tends to zero, leaving just the Hilbert transform term:

$$V(x,t) = \frac{k}{\pi}\fint_{-\infty}^{\infty}\frac{p_{a\xi}}{\xi - x}\mathrm{d}\xi. \tag{79}$$

With this simpler expression, we recover an explicit relation between the vertical component of air velocity on the substrate–air interface and the air layer pressure. Therefore, we need not solve anything separately inside the substrate. The system becomes

$$F_t = \frac{1}{12}\frac{\partial}{\partial x}\left(\frac{\gamma F^4 + 4k^{\frac{1}{2}}F^3}{\gamma F + k^{\frac{1}{2}}}\frac{\partial p_a}{\partial x}\right) + \frac{k}{\pi}\fint_{-\infty}^{\infty}\frac{p_{a\xi}}{\xi - x}\mathrm{d}\xi; \tag{80}$$

$$F_{tt} = -p_{a_{xx}} \qquad x \in \mathbb{R}. \tag{81}$$

This completes the theory. In the next section, we discuss a numerical method used to solve the model's equations and then present results from our computations.

3 Numerical method and results

3.1 Numerical solution

Our problem of interest has now been reduced to two main cases. First, the thin porous layer is governed by coupled equations (61) and (62), along with initial conditions on the interface $y = F(x,t)$ and the air pressure $p_a(x,t)$. We also require that the air–water interface is undisturbed far from the site of impact, so that $F(x,t) \sim x^2/2 - t$ and $p_a(x,t) \to 0$ as $x \to \pm\infty$. In this regime, the flow inside the substrate is essentially passive, driven by the pressure-continuity condition at $y = 0$. We are left with a pair of coupled equations to solve first and then the induced substrate flow can be calculated subsequently. The numerical method we adopted to compute the solution uses a fourth-order finite-difference scheme to discretise the two differential equations. The solution was found by iterating F and p_a at each time step, with (62) firstly giving an updated interface position F and (61) then updating the pressure, p_a. At each time step, it was found that fewer than five iterations are needed to achieve a numerically converged solution, within a typical relative error of 10^{-6}. The grid size and time step size were typically $\delta x = 0.016$ and $\delta t = 10^{-3}$, with smaller values used as a numerical check. We truncated the domain in the far field when applying the boundary conditions. It was found that $x \in [-32, 32]$ was a wide enough truncation to no longer affect the solutions and encompass the decay towards zero in the air pressure with increasing distance from the line of symmetry. Finally, the computations were started at an early enough time, $t = -25$; this value was checked to ensure solutions were independent of the choice of start time.

For the second regime with intermediate-depth porous substrate governed by (76)–(78), our approach was more elaborate. Attempting the same discretisation approach detailed above, the numerics either failed to converge or required prohibitively small grid sizes. Instead, a Fast Fourier Transform method for solving this system was adopted which proved to be stable and close in computational speed to our method for the first regime. We introduce the discrete Fourier expansions of the unknown functions p_a, F and v_s, defined by

$$p_a(x,t) = \sum_{n=1}^{N} P_n(t) e^{\frac{in\pi x}{L}}, \tag{82}$$

$$F(x,t) = \frac{x^2}{2} - t + \sum_{n=1}^{N} F_n(t) e^{\frac{in\pi x}{L}}, \tag{83}$$

$$V(x,t) = \sum_{n=1}^{N} V_n(t) e^{\frac{in\pi x}{L}}, \tag{84}$$

where $x = \pm L$ is the limit of the truncated computational domain. From (73), we have that

$$V(x,t) = \frac{1}{\pi}\left(P.V.\int_{-\infty}^{\infty} \frac{k\frac{\partial p_a(\xi,t)}{\partial \xi}}{\xi - x}\mathrm{d}\xi - \int_{-\infty}^{\infty} \frac{k(\xi - x)\frac{\partial p_a(\xi,t)}{\partial \xi}}{(\xi - x)^2 + 4H_{\text{in}}^2}\mathrm{d}\xi \right.$$
$$\left. - \int_{-\infty}^{\infty} \frac{2H_{\text{in}}V(\xi,t)}{(\xi - x)^2 + 4H_{\text{in}}^2}\mathrm{d}\xi \right), \tag{85}$$

with the help of Gradshteyn and Ryzhik [42] to find exact expressions for the integrals, we substitute the Fourier expansions (82)–(84) and write V_n explicitly in terms of P_n:

$$V_n = -\frac{k|n|\pi}{L}P_n + \frac{k|n|\pi}{L}e^{\frac{-2H_{\text{in}}|n|\pi}{L}}P_n - e^{\frac{-2H_{\text{in}}|n|\pi}{L}}V_n \tag{86}$$

$$\left(1 + e^{\frac{-2H_{\text{in}}|n|\pi}{L}}\right)V_n = \left(-\frac{k|n|\pi}{L} + \frac{k|n|\pi}{L}e^{\frac{-2H_{\text{in}}|n|\pi}{L}}\right)P_n. \tag{87}$$

Note that we have kept these expansions general at this stage to allow for non-symmetric impacts, although in what follows we exploit the fact that F and p_a are even functions of x to reduce the number of unknown coefficients. At each time step, we calculate the set of P_n from the values at the previous time step, then use relation (78) to update F_n:

$$F_{ntt} = \frac{n^2\pi^2}{L^2}P_n, \tag{88}$$

where we discretise F_{ntt} using standard fourth-order finite differences. We use these to update V_n via (87) and exploit relation (76) to update the pressure. We also monitor the relative error between successive iterations. We iterate this process until it converges to a relative error of less than $\pm\ 10^{-6}$. Typically, we truncate to $N = 2001$ terms in each series to give accurate resolution and less than five iterations were needed at each time step to reach convergence. Full details of the discretisation and methods used can be found in [36].

In the next two sections we present results for the two regimes' theories: shallow- and intermediate-depth substrates.

3.2 Shallow porous substrate results

In this section, we present results using the shallow substrate theory of Sect. 2.3.3 part I, in which the substrate has depth $H^* = \epsilon^2 R H_{\text{sh}}$. We begin with the reference case of a wholly impermeable substrate ($k = 0$). Then, we show results for a selection of pairs of values of porosity k and shallow substrate depth H_{sh}. At the end, we draw together some trends in the influence of porosity on the results and contrast them with what happens for an impermeable plate.

We describe results for the right half only $x \geq 0$ of the symmetrical domain. We plot in dimensionless units the free surface, pressure, and pressure gradients.

Typically, a sequence of profiles is shown at unequally separated instants in time. The computations start at $t = -25$ when the wetted body is far above the substrate, and we show developments at times just before impact. We continue computing until the interface is due to meet the substrate at a touchdown time denoted $t = t_0$. In our results $t_0 > 0$ due to the pressurised air layer pushing up against the water film on the cylinder and so delaying the arrival of the interface at $y = 0$ which in the absence of air cushioning is at $t = 0$. When a bubble is captured in the interval between $x = \pm r_b$, its half width is r_b. For short, we say a bubble has *radius* r_b.

As a test of our numerical methods and to show a baseline of results with which to compare the porous substrates that follow, we first present the solution for impact onto an impermeable substrate. Figure 2a shows the evolution of the free-surface and pressure distribution for approach to impact against an impermeable plate at $y = 0$ (porosity $k = 0$). The interface descends and changes shape, capturing a pocket of air against the plate to form a bubble of radius $r_b = 3.0$ to two significant figures. Considering only the right half of the domain, a tongue of liquid descends to define the right-hand edge of the bubble and the tip of the tongue will reach the plate at a positive instant $t = t_0$. Physically, touchdown is delayed due to film spreading and air cushioning. The touchdown time is approximately $t_0 = 0.33$. Figure 3 shows the separation distance from the lowest point of the tongue down to the plate, as a function of time. In vacuo, the trajectory shows constant speed of descent and is the dashed straight line of slope -1. The plot shows an early deceleration (a reduction in gradient), followed by an acceleration (high gradient) towards the time of impact at the touchdown time $t = t_0$. This slowing down then speeding-up happens during the short time when the interface is very close to the plate. As the interface descends it sharpens into a falling tongue of water, as shown in Fig. 2a, b left panels. Figure 2a, b right panels show the simultaneous pressure distribution. The pressure is largest inside the air pocket, with a global maximum pressure at $x = 0$ and spatially it declines steeply near the tongue. Just before touchdown, an elevated pressure spike appears close to the touchdown position. First identified in Korobkin et al. [33] which our results recreate, this differs from reported behaviours during impact of air-cushioned liquid droplets and deep-water layers, where more distinctive local pressure peaks appear near touchdown.

Shallow substrate results are relatively insensitive to changes in H_{sh} because the theory rests on scalings which make the influence of the substrate's bed strong everywhere—the air flow in the substrate is constrained to being predominantly horizontal. So we fix the value $H_{\text{sh}} = 4$ and, through the following examples, increase k from $k = 0$ (impermeable, discussed above), up to $k = 4$.

What happens if the substrate is made slightly permeable? See Fig. 4. With $k = 0.25$ and $H_{\text{sh}} = 4$, the free surface captures a smaller bubble than the impermeable plate. The bubble radius is about $r_b = 2.9$. The bubble is smaller owing to a loss of air pushed into the substrate and then away to the sides. Since the air in the model is incompressible, it also exits the substrate, primarily at the tongue and just outside the bubble, as an air jet. Equation (56) shows the link between p_{axx} and v_s: Fig. 4 (lower-right panel) shows a distinct and growing maximum in p_{axx}, which marks the air jet. The descending water tongue is slowed down by the air pressure. Its touchdown time $t_0 = 1.6$ is about four times later than for the impermeable plate, $t_0 = 0.33$. Overall,

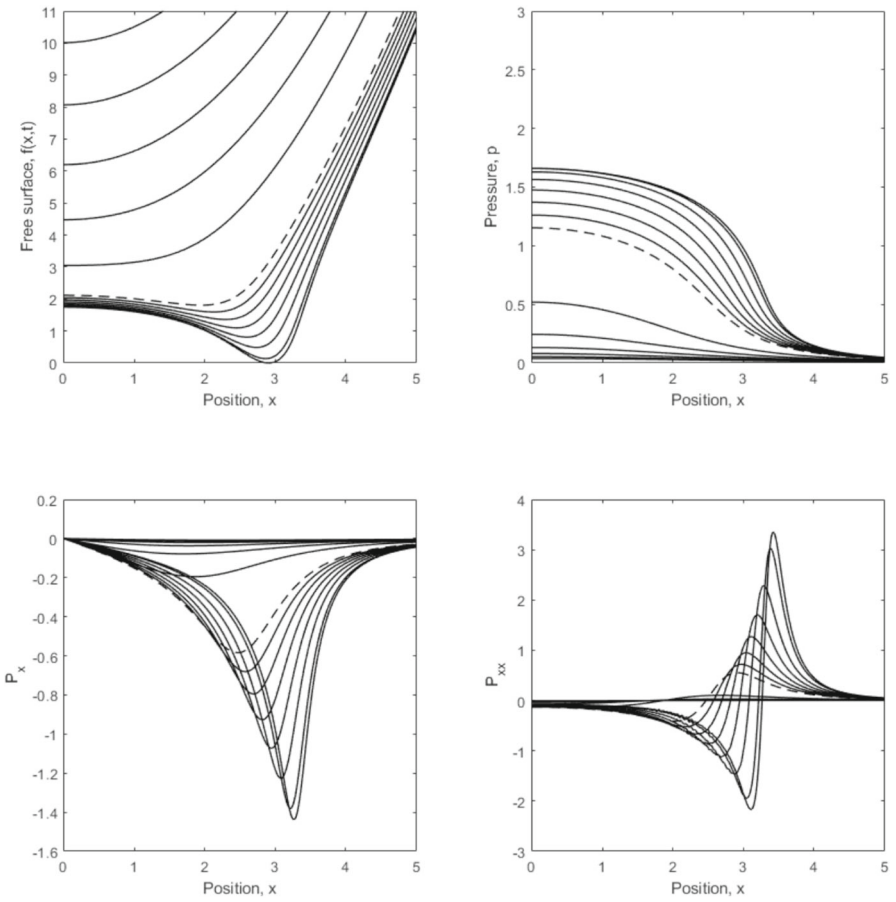

Fig. 4 Free-surface and pressures profiles for $k = 0.25$ and $H_{\text{sh}} = 4$, touchdown time $t_0 = 1.6$. A dashed curve marks $t = 0$. Profiles drawn at times $t = -10, -8, -6, -4, -2, 0$ then $t = 0, 0.25, 0.50, ..., 1.25, 1.50$

the air pressure is reduced in the presence of substrate porosity: the maximum value of p_a occurs at $x = 0$, with magnitude of about 1.6, and still rising at the last time computed.

What happens to the results if the substrate is made more permeable? See Fig. 5. With $k = 2$ and $H_{\text{sh}} = 4$, the interface has caught a narrower and thinner bubble. This tongue is the most slowed down of the examples computed, and its lowest point makes touchdown time $t_0 = 2.1$ (see Fig. 7), (about six times the value of $t_0 = 0.36$ for $k = 0$). Pressure is reduced further by this increase in permeability: the maximum value occurs at $x = 0$, where $p_a = 0.6$ (and rising) at the last time computed.

See Fig. 6. A further increase in permeability to $k = 4$ and $H_{\text{sh}} = 4$ gives the results shown in Fig. 6. Now there is no bubble capture; the pressure maximum is only 0.4, and the touchdown time is reduced to about $t_0 = 1.2$. This marks a reduced deceleration of the point of first contact on the interface, descending along the centreline. The air

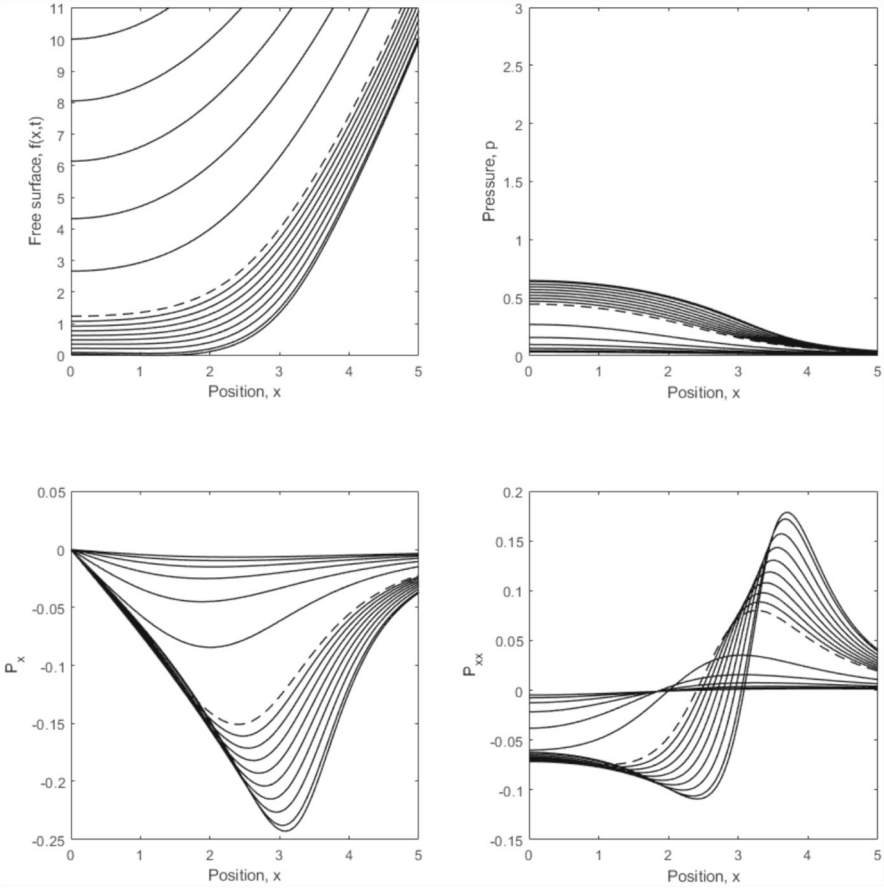

Fig. 5 Free-surface and pressures profiles for $k = 2$ and $H_{\text{sh}} = 4$, touchdown time $t_0 = 2.1$. A dashed curve marks $t = 0$. Profiles drawn at times $t = -10, -8, ..., -2, 0$ then $t = 0, 0.25, 0.50, ..., 2.0$

flows mainly horizontally in both the air layer and inside the substrate. These flows are also slower due to the reduced pressure gradients shown in panels 2,3,4 of Fig. 6.

See Figs. 7 and 8. We now pause to synthesise these shallow substrate results across the two-dimensional parameter space of k, H_{sh}. In Fig. 7, we have contours of constant (marked) touchdown time, t_0. Note the ridge of elevated values in the middle-right part of the plot where $t_0 \geq 2.2$. For a fixed value of H_{sh}, if we increase k from zero vertically up the plot, we find a local maximum in t_0 for some value of k. From the results discussed above t_0 can be as high as 2.3, for $k = 1.4$ and $H_{\text{sh}} = 4$. The shallow substrate theory resolves a region of parameter space where t_0 has a local maximum as a function of k and fixed $H_{\text{sh}} > 1.5$. This supplements the results reported by Hicks and Purvis [23]; with an intermediate-depth theory and fixed depth, they report a *monotone decrease* in t_0 with increasing k.

Figure 8 shows a contour plot of the bubble's radius, r_b, as a function of k and H_{sh} for the same region of parameter space. There is an unbounded region in the

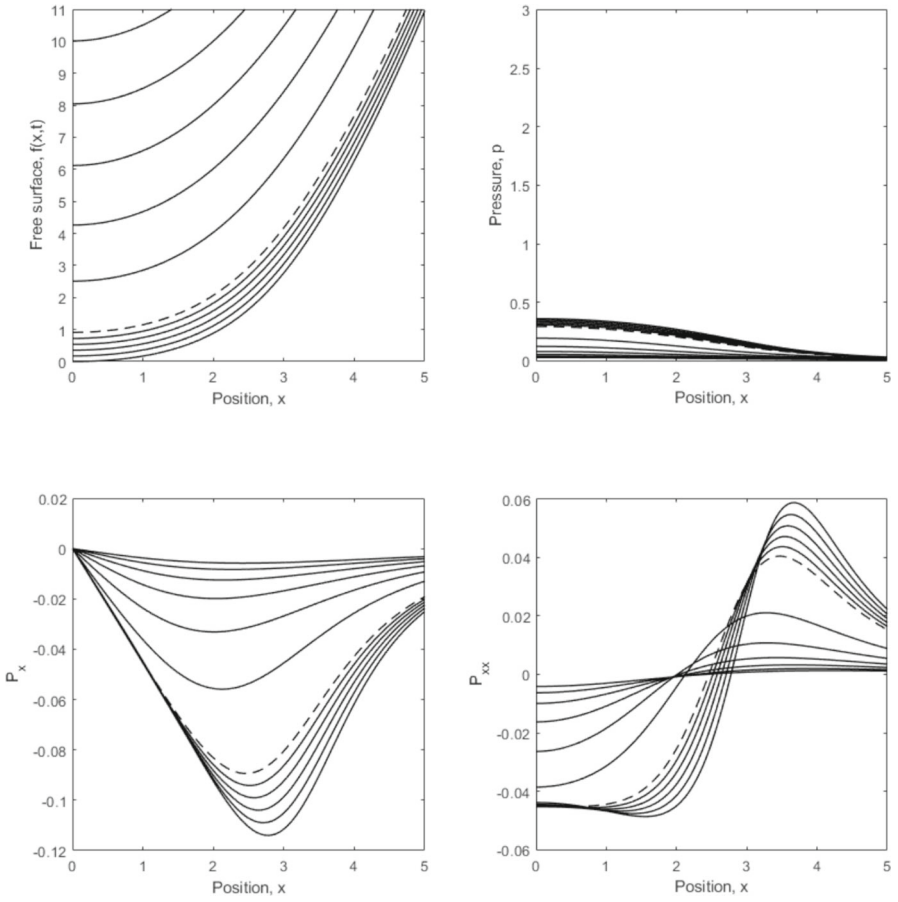

Fig. 6 Free-surface and pressures profiles for $k = 4$ and $H_{\text{sh}} = 4$, touchdown time $t_0 = 1.2$. Profiles drawn at times $t = -10, -8, ..., -2, 0$ then $t = 0, 0.2, 0.4, ..., 1.0$

top-right corner of the plot, where $kH_{\text{sh}} > 10$, in which there is no bubble. This region corresponds to conditions in which the air layer can most easily escape the descending water film, either to the sides or into and along the substrate. In Eq. (56), the vertical component of air velocity into the substrate is directly proportional to kH_{sh}. The presence or absence of a bubble has a strong influence on what will happen next to the water impacting onto and into the substrate.

The boundary between bubble and no bubble occurs at about $kH_{\text{sh}} = 10$, according to our shallow substrate computations. In the remaining region of the plot, a bubble *is* caught when approximately $kH_{\text{sh}} \leq 10$. The bubble radius r_b is increased by reducing k: the radius increases up to a maximum $r_b = 3.0$ for the impermeable plate, $k = 0$.

Figure 9 shows another synthesis of results: the trajectory of the lowest free-surface point. A broad conclusion is that (at a fixed depth of substrate) the effects of increasing k are to relax the acceleration and deceleration of the approaching air–water interface.

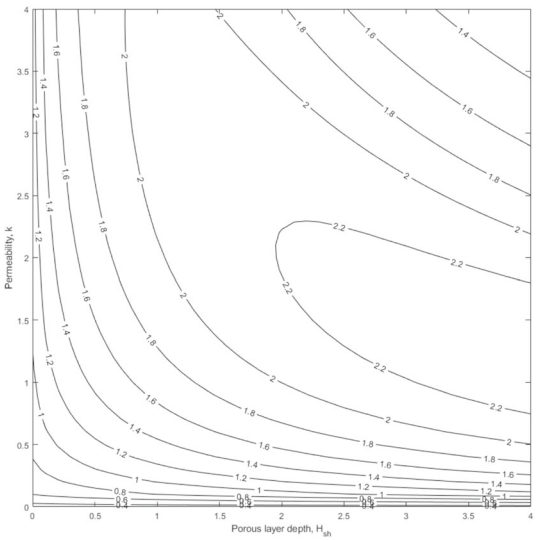

Fig. 7 Contours of touchdown time, t_0, as a function of k (vertical axis) and H_{sh}

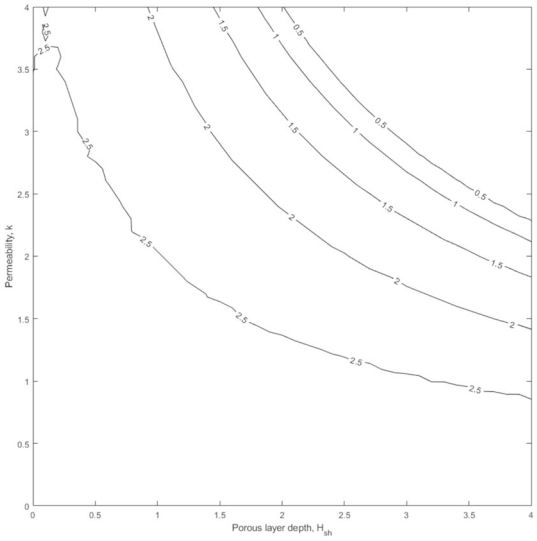

Fig. 8 Contours of bubble radius, r_b, as a function of k (vertical axis) and H_{sh}

The air finds it ever easier to escape into the pores of the substrate and or to move sideways away from the descending tongue.

We also discuss plots of the air's volume fluxes. See Fig. 10. The horizontal volume flux, HVF, is defined as that crossing a geometrical vertical line segment, drawn from the lowest point on the tongue to the top of the substrate (see Eq. (63)). Calculations start when we begin to have a distinct tongue. As the descending minimum point of the tongue moves to the right, $x = l(t)$ also moves to the right. The curve shows that as time increases HVF increases from zero to a positive maximum, with flow to the right; after which HVF declines. Also plotted in Fig. 10 is the vertically downward

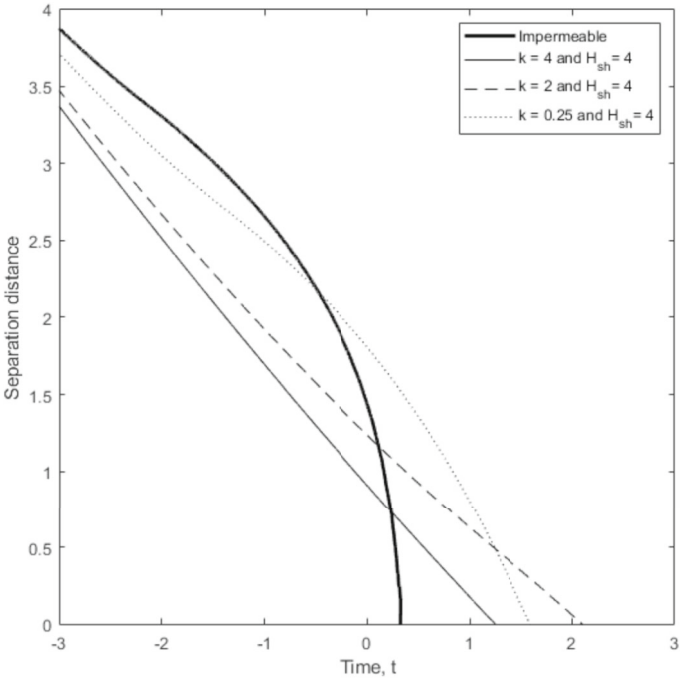

Fig. 9 In the shallow porous regime, separation distance between lowest point on free surface and top of substrate: plots for various values of k and fixed $H_{\text{sh}} = 4$

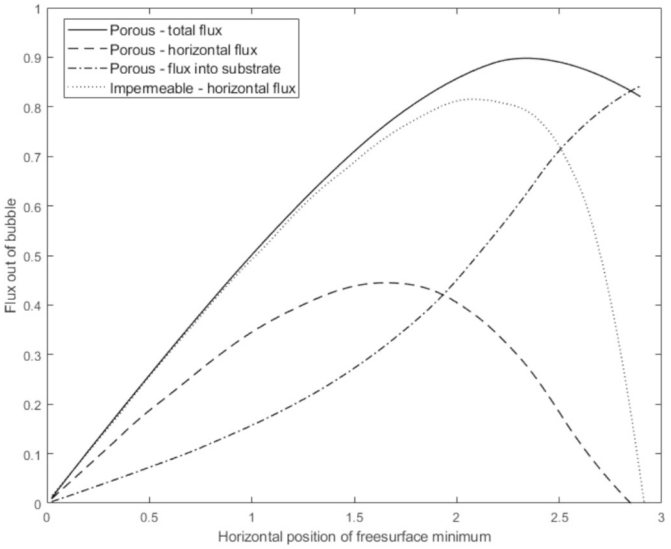

Fig. 10 For the shallow porous model, plots of horizontal volume flux, vertical volume flux out of the bubble, and total flux, as functions of x-coordinate of the minimum of the liquid surface drawn for $H_{\text{sh}} = 4$ and $k = 0.5$. Horizontal flux for impermeable substrate, $k = 0$, is also shown

volume flux, VVF, computed at the top of the substrate between the centreline and the tongue's position (see Eq. (64)). VVF measures the volume of air entering the substrate in the interval $[0, l(t)]$. The main contribution comes from the falling tongue pushing air into the substrate. The curve shows a monotone increase over time, from zero to a maximum whose magnitude is similar to that of HVF. Both HVF and VVF have been computed for $k = 0$ (impermeable) and $k = 0.5$ in shallow substrate $H_{\text{sh}} = 4$. By considering a slightly porous substrate, we see that the main contribution to the total flux (also plotted) is from the horizontal flux during the early approach to touchdown. But as the film approaches impact, the air pressure in the bubble continues to rise, allowing more air to be forced vertically down into the substrate, and the horizontal flux declines. Increasing the porosity makes VVF become greater than HVF much earlier.

Overall, under the water tongue there is a horizontal air flow to the right, caused by the bubble (on the left side of the tongue) shrinking in volume due to the water layer pushing down on it. Some air escapes under the tongue, then off to the right, and some air penetrates the substrate.

3.3 Intermediate-depth porous substrate results

Here, the results come from theory Sect. 2.3.3 part II, in which the substrate depth is $H^* = \epsilon R H_{\text{in}}$. Unlike the previous section, we now have a fully two-dimensional velocity field inside the substrate. The air is free to move in a region which is as deep as it is broad, and whose length scale, ϵR, equals the width of the zone of high air pressure for the wetted cylinder approaching the substrate. Figures 11, 12, 13, and 14 show various profiles, exploring significant parts of the k, H_{in} parameter space.

First, what happens if the substrate is made slightly permeable? Does the greater depth scale of the theory make a significant change in the results? Let $k = 0.25$ and we set $H_{\text{in}} = 0.25$, which is already physically deeper than the cases of shallow substrate presented in the previous Sect. 3.2. The top left panel in Fig. 11 shows that the free surface captures a wide bubble. The tongue is slowed down by the air pressure and then accelerates into touchdown. It will make contact with the substrate at time $t_0 = 1.1$, (about triple the value of $t_0 = 0.33$ for $k = 0$). The pressure in Fig. 11, top-right panel, is reduced by the substrate: its maximum p_a occurs at $x = 0$ and has magnitude about 2.3 and still rising at the last time computed. The vertical velocity distribution at $y = 0$ is sensitive to the second-x-derivative of pressure, and $p_{a_{xx}}$ changes sign either side of the descending tongue. Near the approaching touchdown point, $x = 2.9$, air enters the substrate just inside the bubble and exits both at the tongue and just outside the bubble. The nearby maximum vertical velocities are as follows. First, into the substrate $v_s = -0.4$; second, out of the substrate $v_s = 0.35$. These maximal speeds are similar, reflecting the notion that incompressible air entering the substrate immediately displaces other air from inside the substrate, forcing the latter to exit. This exit flow from the substrate is so narrow that we can call it an 'air jet' (or 'air splash'). Its speed, at the jet root, is still growing at the last time computed.

For the next case, we increase the permeability to $k = 1$ and maintain the depth at $H_{\text{in}} = 1$. See Fig. 12. The bubble radius $r_b = 2.8$. The pressure's spatial maximum is

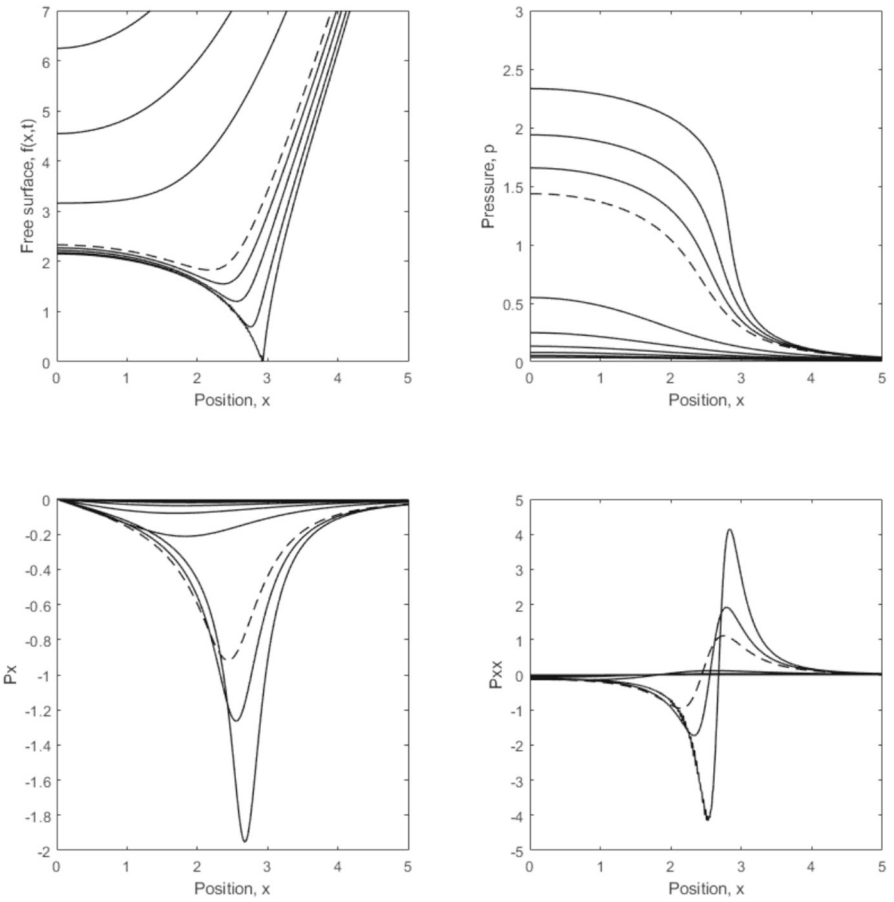

Fig. 11 Intermediate-depth porous model. Free surface, pressure, and pressure gradients for $k = 0.25$ and $H_{\text{in}} = 0.25$. The dashed curve is at $t = 0$. Profiles drawn at times $t = -6, -4, -2, 0$ then $t = 0, 0.25, 0.50, ..., 1.0$. Touchdown occurs at $t_0 = 1.1$

about 2.2 and still rising. The vertical velocity at $y = 0$ is about ± 0.21. Touchdown occurs at $t_0 = 1.3$.

Next, we increase the permeability and reduce the depth: $k = 2$ and $H_{\text{in}} = 0.25$. See Fig. 13. The bubble radius is $r_b = 2.6$. The still rising pressure maximum is about 1.7. The vertical velocity v_s at $y = 0$ is about ± 0.9. Touchdown occurs at a later time of $t_0 = 1.4$. Equation (56) shows the link between p_{axx} and v_s: the lower-right panel shows a distinct and growing maximum in p_{axx}, which marks the air jet.

Finally, we treat an infinitely deep substrate using a suitably adapted numerical method: $k = 0.1$ and $H_{\text{in}} \to \infty$, as shown in Fig. 15. During its descent, the tongue moves to the right, eventually capturing a bubble of radius r_b about 3.0. The growing pressure reaches a maximum of about 1.9. The vertical velocity at $y = 0$ ranges between about -1 (downward flow) and about 0.4 (upward-exiting flow). Touchdown occurs at $t_0 = 1.1$. One contribution to the increase in t_0 is the initial height of that

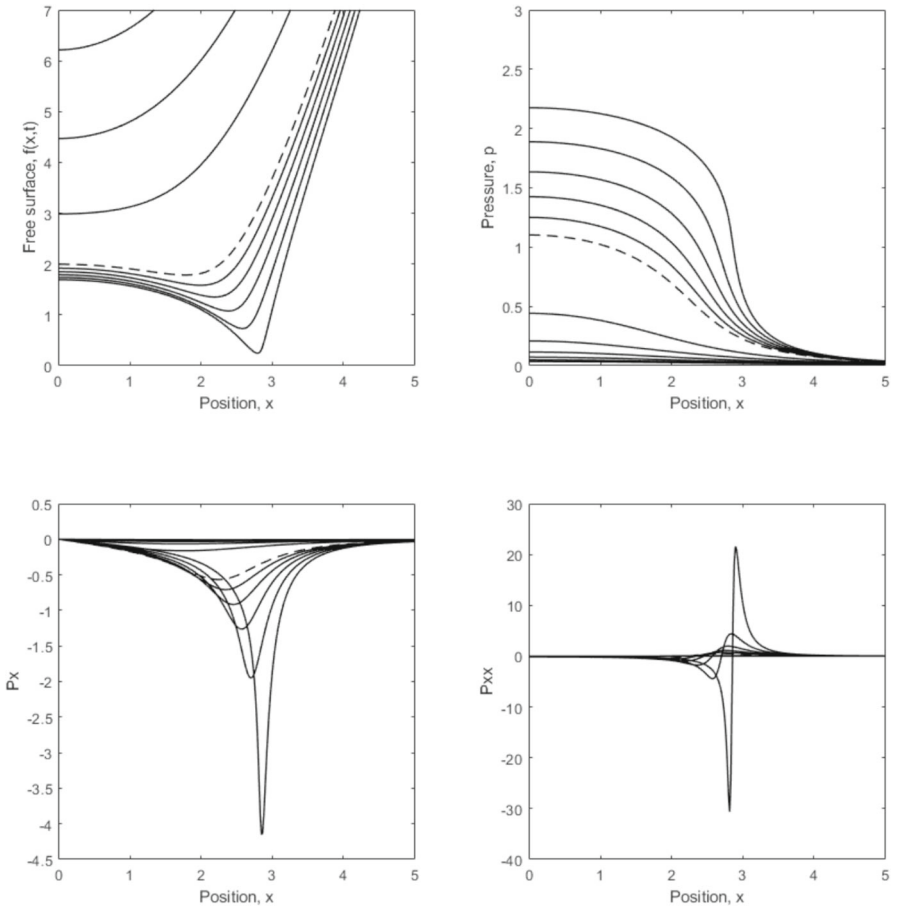

Fig. 12 Intermediate-depth porous model. Free surface, pressure, and pressure gradients for $k = 1$ and $H_{\text{in}} = 0.25$. The dashed curve is at $t = 0$. Profiles drawn at times $t = -6, -4, -2, 0$ then $t = 0, 0.25, ..., 1.25$. Touchdown is at $t_0 = 1.3$

part of the free surface which forms a tongue and descends onto the substrate. For touchdown to occur at the centre, $x = 0$, we expect t_0 to have a smaller value than for a bubble-capturing tongue, because the tongue needs more time to descend further to reach the substrate.

4 Conclusions and further work

4.1 Conclusion

We established in Sect. 2 a mathematical model comprising symmetric two-dimensional coupled flows (water film, air layer, and air-porous substrate) forced by the descent of a wetted cylinder towards impact with a porous solid substrate. One

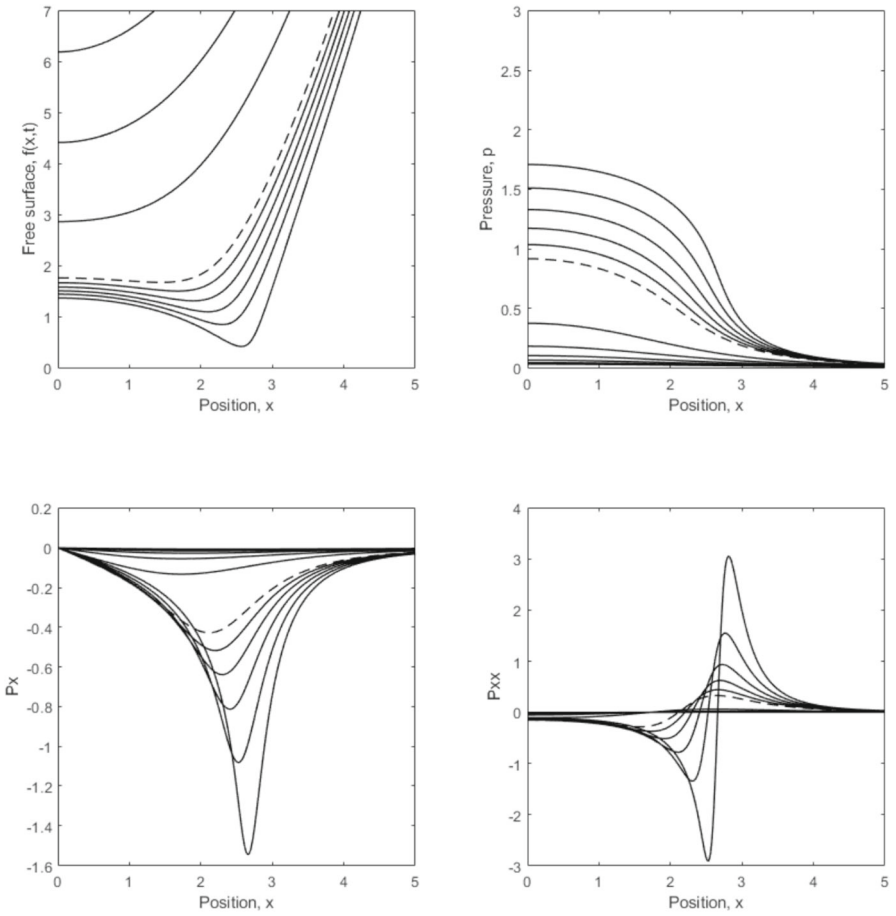

Fig. 13 Intermediate-depth porous model. Free surface, pressure, and pressure gradients for $k = 2$ and $H_{\text{in}} = 0.25$. The dashed curve is at $t = 0$. Profiles drawn at times $t = -6, -4, -2, 0$ then $t = 0, 0.2, 0.4, ..., 1.2$, where $t_0 = 1.4$

novel feature of our work is in identifying an asymptotic scaling for the model variables which achieves a consistent balance between the chief terms in the complicated full equations of motion and boundary conditions. We solve the coupled equations numerically with two methods: a fourth-order finite differences scheme and a Fourier representation (spectral) method, truncated at 2001 terms. Both methods work efficiently in that they are robust, quickly converge, and produce consistent accurate estimates of the unique solution in each case.

The model has two independent dimensionless parameters: a substrate porosity k and a substrate depth H (either H_{sh} or H_{in}). Regions of k, H space are explored through case-by-case examples. The water film either captures no bubble or one bubble, with an associated air flow forced into, and displaced out of, the substrate.

In k, H_{sh} space, a contour plot of the half width (radius) r_b of the bubble makes clear the regime of bubble capture and confirms a maximum value of r_b for impermeable

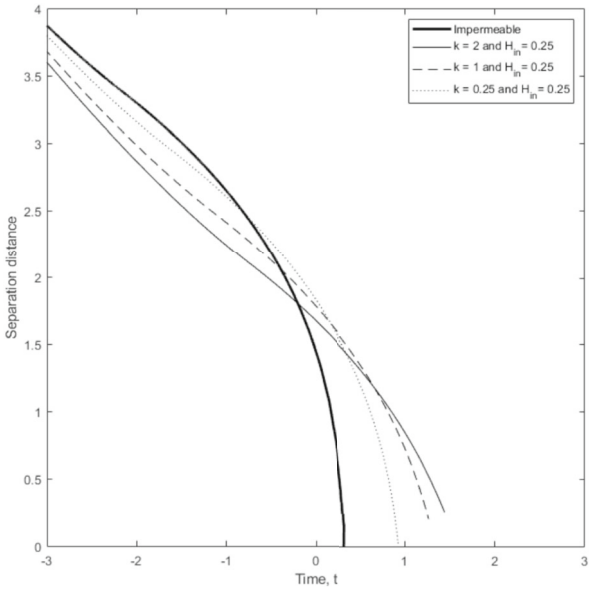

Fig. 14 Intermediate-depth substrates: separation distances versus time. Note acceleration of the film interface into touchdown plotted for 4 pairs of k and H_{in}

substrate. Figure 8 shows two regions: at lower left, bubbles are formed; at upper right is a blank region of no bubble.

Figure 7 is a second contour plot in k, H_{sh} space, of touchdown time t_0 (when the water surface meets the substrate top) and this was explored. At fixed depth, as k rises from zero, t_0 increases to a local maximum and then decreases. This is a new finding and contrasts with a monotone decreasing t_0 reported by Hicks and Purvis [23].

Computational results report examples of an impermeable, shallow (relative to the width of the impact zone), intermediate-depth, and deep substrate. When an air bubble occurs, it is captured between the water film and substrate by two symmetrically placed tongues of water that descend faster than the rest of the initially parabolic water surface. It is the lowest point of the tongues that first meets the substrate to define a touchdown time, t_0. The spatial and temporal details of the tongues are well resolved by the method.

Another new feature of the results is the presence of air jets. Air pushed into the substrate can also exit as a jet, especially when H_{sh} is small enough. The vertical component of velocity at the substrate surface, $v_s(x, 0, t)$, is greatest in a narrow x interval that lies from under the tongue to just inside the bubble, where air is forced in. And air exits most quickly just outside the bubble as an air jet. The maximum magnitude of $v_s(x, 0, t)$ is no more than the particle's speed of descent and is absolutely small everywhere else.

When there is no bubble, the air is free enough to either go into the substrate or flee to the sides, with little evidence of any air jet. Under these circumstances, the air layer pressure is so low that it hardly affects the shape of the water surface and impedes very little its descent towards the substrate. Without a bubble, touchdown occurs first at the centre of the impact zone.

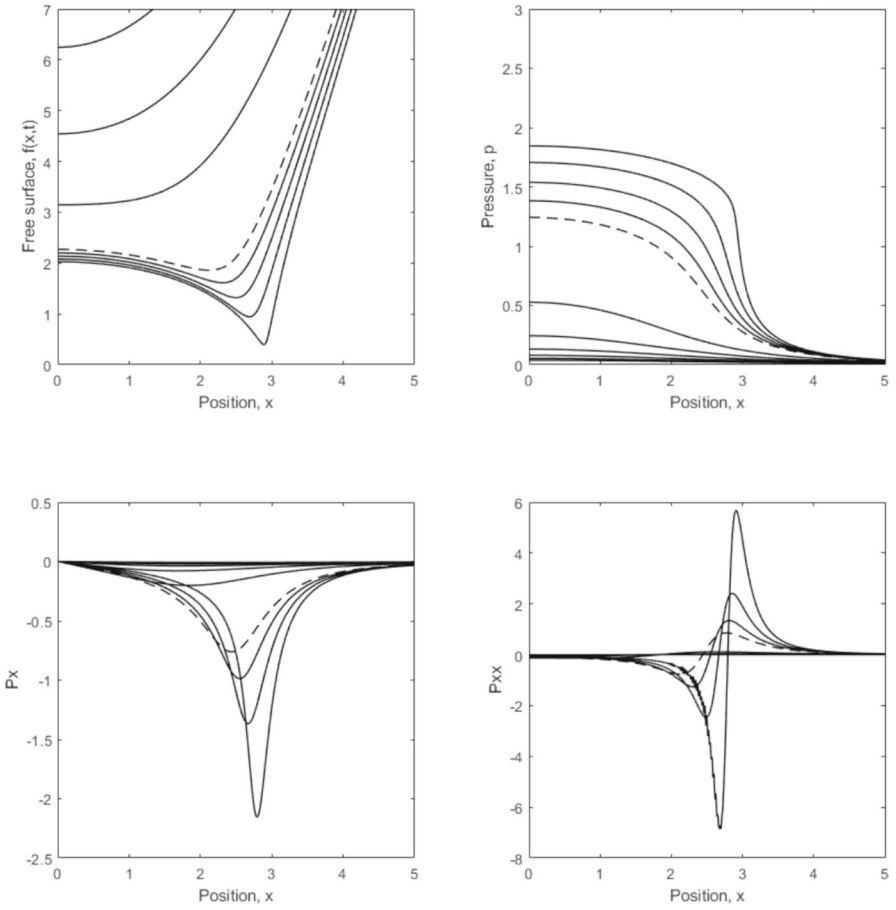

Fig. 15 Infinite-depth substrate: profiles for $k = 0.1$. Profiles drawn at times $t = -6, -4, -2, 0$ then $t = 0, 0.25, 0.50, ..., 1.0$, where $t_0 = 1.1$

Our model and results can equally well be interpreted for the descent towards impact of a *porous particle* approaching the water surface of a liquid film coating an *impermeable substrate*. Such a scenario is closer to a food manufacturing setting, e.g. porous seeds sprinkled onto the top of a moist solid foodstuff.

4.2 Future research and open questions

We revisit the assumptions made in the modelling: (a) the high Bond number suggested we neglect surface tension from the air–water interface. Including capillarity and small pressure differences across the interface would not change our primary high-pressure scaling balance of constants $P_a = P_w$. Indeed, using the FFT representation, it is straightforward to include the curvature term of capillarity in the free-surface shape. Preliminary computations show that the influence of capillarity is to delay the arrival

of the water tongue at the substrate and the right-hand tongue's lower surface can skate towards the right on top of a layer of high-pressure air. (b) Geometry: our model is two-dimensional. An axisymmetric flow domain is more natural, e.g. for a spherical ice particle impact, see Hicks et al. [43]. (c) Air compressibility: Hicks and Purvis ([22]) have looked at this for impermeable substrates. (d) Symmetry: the incident particle could be impacting at an oblique angle away from approach along the normal to the substrate. Moreton [36] showed that the approach must be close to horizontal to see significant asymmetry in the pressure distribution for an impermeable plate. (e) Substrate: Most real porous substrates are inhomogeneous and anisotropic. Both of these can be accommodated within a Darcy flow model by making K into a matrix of elements depending on position within the substrate. Pre-saturated substrates are also of great practical interest, but offer a formidable challenge to model. (f) Dirty liquid/gas: can micro-organisms and dust particles be driven into the substrate? (g) Liquid viscosity: is there a regime in which the liquid film's viscosity is significant?

This work can supply consistent initial conditions for future modelling of the impact of a water layer onto and into a substrate. Where will the free air–water interface go as an advancing wetting front? What new conditions pertain inside the substrate? We anticipate that each bubble computed in the present work will strongly affect the subsequent motion of the wetting front inside the substrate. Our approach through modelling a very shallow substrate in Sect. 2.3.3 part I has many simplifying advantages. Such a model could relegate the vertical velocity component to satisfying the mass-continuity equation and would allow us to predict a simple wetting front whose right half advances to the right with a time-dependent depth-uniform horizontal velocity, coupled to a pressure field that is primarily dependent on x. Film impact into an intermediate-depth substrate (Sect. 2.3.3 part II) would be much more difficult to model, owing to the fully two-dimensional, time-dependent velocity field and its free-surface wetting front.

A major challenge remains describing the transition between pre-impact air cushioning of the type described here and post-impact liquid flow into the porous substrate and the lateral spreading of a splash jet. An initial attempt at modelling the equivalent post-impact behaviour using only an ansatz boundary condition was carried out in Moreton et al. [35]. Two important open questions are as follows: how does air cushioning continue to influence the liquid flow once touchdown has occurred, both inside the substrate and in the lubrication film? And what is the longer-term fate of the air bubble?

Appendix A Integral equation for the Darcy flow in an intermediate-depth substrate

Here, we present some complex analysis derivation of the integral equation for the Darcy flow induced in the porous layer by the air layer pressure for the intermediate-depth case defined by (68–72).

We use an image system to solve Laplace's equation in the substrate. We solve it in a rectangular region of depth H_{in}, with zero normal component of velocity at the base of the substrate ($v_s = 0$ at $y = -H_{\text{in}}$) and air pressures equal at the air–substrate interface. We reflect this rectangle in the base of the substrate and use Cauchy's integral

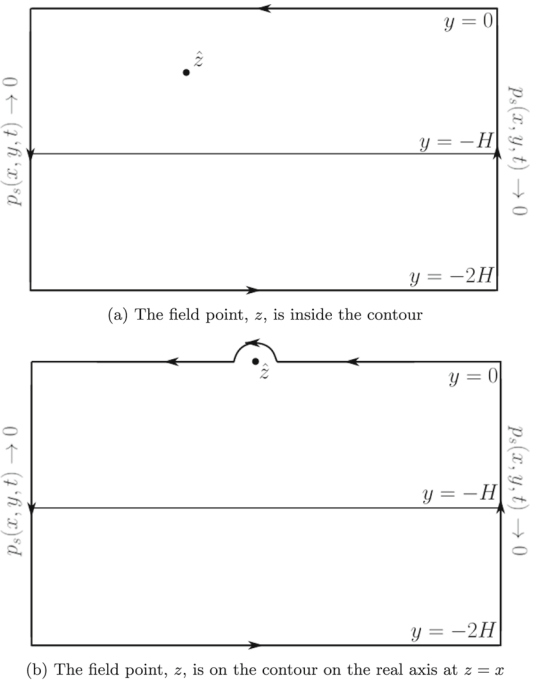

(a) The field point, z, is inside the contour

(b) The field point, z, is on the contour on the real axis at $z = x$

Fig. 16 Diagrams showing the contour of integration, Γ, around the porous layer, and its reflection in $y = -H_{\text{in}}$ depending on where field point z lies

formula to derive an integral equation for v_s. Let complex variable $z = x + iy$ and we define complex-valued function $w(z, t)$ by

$$w(z, t) = k p_{s_x}(z, t) + i v_s(z, t). \tag{A1}$$

Here, w is analytic because $k p_{s_x}$ and v_s satisfy the Cauchy–Riemann relations. We next use Cauchy's integral formula with a contour of integration Γ as shown in Fig. 16 and defined as the perimeter of a rectangular region described anticlockwise, we have

$$w(z, t) = \frac{1}{2\pi i} \oint_{\Gamma} \frac{w(\zeta, t)}{\zeta - z} \mathrm{d}\zeta, \tag{A2}$$

The contribution from integrals at $x = \pm\infty$ is zero because, as we extend in the horizontal direction the integrand tends to zero exponentially. Here, we have different forms of this contour integral depending on whether the field point z lies on Γ or not. If z lies strictly inside Γ then

$$w(z, t) = \frac{1}{2\pi i} \left(\int_{\infty}^{-\infty} \frac{w(\xi, t)}{\xi - z} \mathrm{d}\xi + \int_{-\infty}^{\infty} \frac{w(\xi, t)}{\xi - 2H_{\text{in}} i - z} \mathrm{d}\xi \right). \tag{A3}$$

If $z = x$, then we must deform Γ around this point, as shown in Fig. 16. From (A2), the factor $\frac{1}{2}$ changes to 1, accommodating the contribution from the semi-circular

indentation shown in the figure, we have a principal value integral from taking the limit of the radius of this indentation to zero. For more details, see Carrier et al. [44].

In (A3), we note that w is known on $y = 0$ and $y = -2H_{\text{in}}$, from the boundary data: $kp_{a_x} + iv_s$ (and its complex conjugate, due to reflection in the bed). We take $Im(z) = 0$, because we are interested in the pressure and velocity at $y = 0$. So we have

$$kp_{s_x} + iv_s = \frac{1}{i\pi}\left(\int_{\infty}^{-\infty} \frac{kp_{a\xi} + iv_s}{\xi - x}\mathrm{d}\xi + \int_{-\infty}^{\infty} \frac{(kp_{a\xi} - iv_s)(\xi - x + 2H_{\text{in}}i)}{(\xi - x)^2 + 4H_{\text{in}}^2}\mathrm{d}\xi\right). \tag{A4}$$

Here, we choose to take the imaginary part to obtain an integral relation between the air velocity on the surface of the substrate and the pressure. (Taking the real part leads to an equivalent expression without advantage.) This leaves the following integral equation:

$$v_s(x,t) = \frac{1}{\pi}\left(\int_{-\infty}^{\infty} \frac{kp_{a\xi}}{\xi - x}\mathrm{d}\xi + \int_{-\infty}^{\infty} \frac{-k(\xi - x)p_{a\xi} - 2H_{\text{in}}v_s(\xi,t)}{(\xi - x)^2 + 4H_{\text{in}}^2}\mathrm{d}\xi\right). \tag{A5}$$

Acknowledgements The authors thank the referees for their constructive and helpful comments in the reviewing process. MJC thanks UEA for research facilities.

Author contributions The three authors shared equally in the initial draft and subsequent editing. The development of the models was done jointly by the three authors and numerical calculations were carried out primarily by GM. Analysis and interpretations of the results were also shared between all authors. The authors also shared equally in making changes for the revised version.

Data availability No datasets were generated or analysed during the current study.

Declarations

Conflict of interest The authors declare no conflict of interest.

References

1. Dam DB, Le Clerc C (2004) Experimental study of the impact of an ink-jet printed droplet on a solid substrate. Phys Fluids 16(9):3403–3414

2. Mazur R, Ryżak M, Sochan A, Beczek M, Polakowski C, Przysucha B, Bieganowski A (2022) Soil deformation after one water-drop impact-the effect of texture and soil moisture content. Geoderma 417:115838
3. Zhang S, Hu X, Lourenço SD (2023) Modelling of water droplet dynamics on hydrophobic soils: a review. In: E3S web of conferences, vol 382, EDP Sciences, p 18005
4. Paredes-Mariño J, Forte P, Alois S, Chan KL, Cigala V, Mueller SB, Poret M, Spanu A, Tomašek I, Tournigand P-Y, Perugini D (2022) The lifecycle of volcanic ash: advances and ongoing challenges. Bull Volcanol 84(51):1–12
5. Cuomo G, Allsop NWH, Bruce T, Pearson J (2010) Breaking wave loads at vertical seawalls and breakwaters. Coast Eng 57(4):424–439
6. Gent RW, Dart NP, Cansdale JT (2000) Aircraft icing. Phil Trans R Soc Lond A 358:2873–2911
7. Maitra T, Antonini C, Tiwari MK, Mularczyk A, Imeri Z, Schoch P, Poulikakos D (2014) Supercooled water drops impacting superhydrophobic textures. Langmuir 30(36):10855–10861
8. Maitra T, Tiwari MK, Antonini C, Schoch P, Jung S, Eberle P, Poulikakos D (2014) On the nanoengineering of superhydrophobic and impalement resistant surface textures below the freezing temperature. Nano Lett 14(1):172–182
9. Purvis R, Smith FT (2016) UK success stories in industrial mathematics. In: Aston PJ, Mulholland AJ, Tant KMM (eds) Improving aircraft safety in icing conditions. Springer, Cham, pp 145–151
10. Palmer RA, Smith FT (2021) A body in nonlinear near-wall shear flow: numerical results for a flat plate. J Fluid Mech 915:35
11. Liu Q, Yazar S, Smith FT (2023) On interaction between freely moving bodies and fluid in a channel flow. Theor Appl Mech Lett 13(1):100413
12. Smith FT, Jolley EM, Palmer RA (2023) On modelling fluid/body interactions, impacts and lift-offs. Acta Mech Sin 39(5):1
13. Thoroddsen ST, Etoh TG, Takehara K (2003) Air entrapment under an impacting drop. J Fluid Mech 478:125–134
14. Li EQ, Thoroddsen ST (2015) Time-resolved imaging of a compressible air disc under a drop impacting on a solid surface. J Fluid Mech 780:636–648
15. Zhao W, Lin S, Chen L, Li E, Thoroddsen ST, Thoraval M (2020) Jetting from an impacting drop containing a particle. Phys Fluids 32:011704
16. Wang X, Xu B, Guo S, Zhao Y, Chen Z (2023) Droplet impacting dynamics: recent progress and future aspects. Adv Coll Interface Sci 317:102919
17. Wilson SK (1991) A mathematical model for the initial stages of fluid impact in the presence of a cushioning fluid layer. J Eng Math 25:265–285
18. Smith FT, Li L, Wu GX (2003) Air cushioning with a lubrication/inviscid balance. J Fluid Mech 482:291–318
19. Vanden-Broeck JM, Smith FT (2008) Surface tension effects on interaction between two fluids near a wall. QJMAM 61:117–128
20. Bouwhuis W, Veen RC, Tran T, Keij DL, Winkels KG, Peters IR, Meer D, Sun C, Snoeijer JH, Lohse D (2012) Maximal air bubble entrainment at liquid-drop impact. Phys Rev Lett 109(26):264501
21. Mani M, Mandre S, Brenner MP (2010) Events before droplet splashing on a solid surface. J Fluid Mech 647:163–185
22. Hicks PD, Purvis R (2013) Liquid-solid impacts with compressible gas cushioning. J Fluid Mech 735:120–149
23. Hicks PD, Purvis R (2015) Gas-cushioned droplet impacts with a thin layer of porous media. J Eng Math 102:65–87
24. Henman NIJ, Smith FT, Tiwari MK (2021) Pre-impact dynamics of a droplet impinging on a deformable surface. Phys Fluids 33(9):092119
25. Pegg M (2019) Impact of liquid droplets with deformable surfaces. PhD thesis, University of East Anglia
26. Srikar R, Gambaryan-Roisman T, Steffes C, Stephan P, Tropea C, Yarin AL (2009) Nanofiber coating of surfaces for intensification of drop or spray impact cooling. Int J Heat Mass Trans 52(25–26):5814–5826
27. Han D, Steckl AJ (2009) Superhydrophobic and oleophobic fibers by coaxial electrospinning. Langmuir 25(16):9454–9462
28. Gilet T, Bourouiba L (2014) Rain-induced ejection of pathogens from leaves: revisiting the hypothesis of splash-on-film using high-speed visualization. Soc Integr Comp Biol 54:974–984

29. Marston JO, Thoroddsen ST, Ng WK, Tan RBH (2010) Experimental study of liquid drop impact onto a powder surface. Powder Technol 203:223–236
30. Tran T, Staat HJJ, Susarrey-Arce A, Foertsch TC, Houselt A, Gardeniers HJGE, Prosperetti A, Lohse D, Sun C (2013) Droplet impact on superheated micro-structured surfaces. Soft Matter 9:3272–3282
31. Tsai P, Veen RCA, Raa M, Lohse D (2010) How micropatterns and air pressure affect splashing on surfaces. Langmuir 26(20):16090–16095
32. Raza MA, Swigchem J, Jansen HP, Zandvliet HJW, Poelsema B, Kooij ES (2014) Droplet impact on hydrophobic surfaces with hierarchical roughness. Surf Topogr Metrol Prop 2(3):035002
33. Korobkin AA, Ellis AS, Smith FT (2008) Trapping of air in impact between a body and shallow water. J Fluid Mech 611:365–394
34. Hicks PD, Crosby A, Hewitt D, Hennessy M, Herterich J, Moyles I (2012) Liquid interactions with porous media and the fate of toxic materials. European Study Group with Industry (ESGI) report
35. Moreton G, Purvis R, Cooker MJ (2024) Droplet impact onto a porous substrate: a Wagner theory for early-stage spreading. J Eng Math 146(1):2
36. Moreton G (2022) Droplet impacts onto porous substrates: pre-and post-impact dynamics. PhD thesis, University of East Anglia
37. Ross S, Hicks PD (2019) A comparison of pre-impact gas cushioning and Wagner theory for liquid-solid impacts. Phys Fluids 31(4):042101
38. Mandre S, Mani M, Brenner MP (2009) Precursors to splashing of liquid droplets on a solid surface. Phys Rev Lett 102(13):134502
39. Beavers GS, Joseph DD (1967) Boundary conditions at a naturally permeable wall. J Fluid Mech 30:197–207
40. Saffman PG (1971) On the boundary condition at the surface of a porous medium. Stud Appl Math 50:93–101
41. Knox DJ, Wilson SK, Duffy BR, McKee S (2015) Porous squeeze-film flow. IMA J Appl Math 80:376–409
42. Gradshteyn IS, Ryzhik IM (2000) Table of integrals, series, and products. Academic Press, Section 3.723, New York
43. Hicks PD, Ermanyuk EV, Gavrilov NV, Purvis R (2012) Air trapping at impact of a rigid sphere onto a liquid. J Fluid Mech 695:310–320
44. Carrier GF, Krook M, Pearson CE (2005) Functions of a complex variable: theory and technique. SIAM, New York